



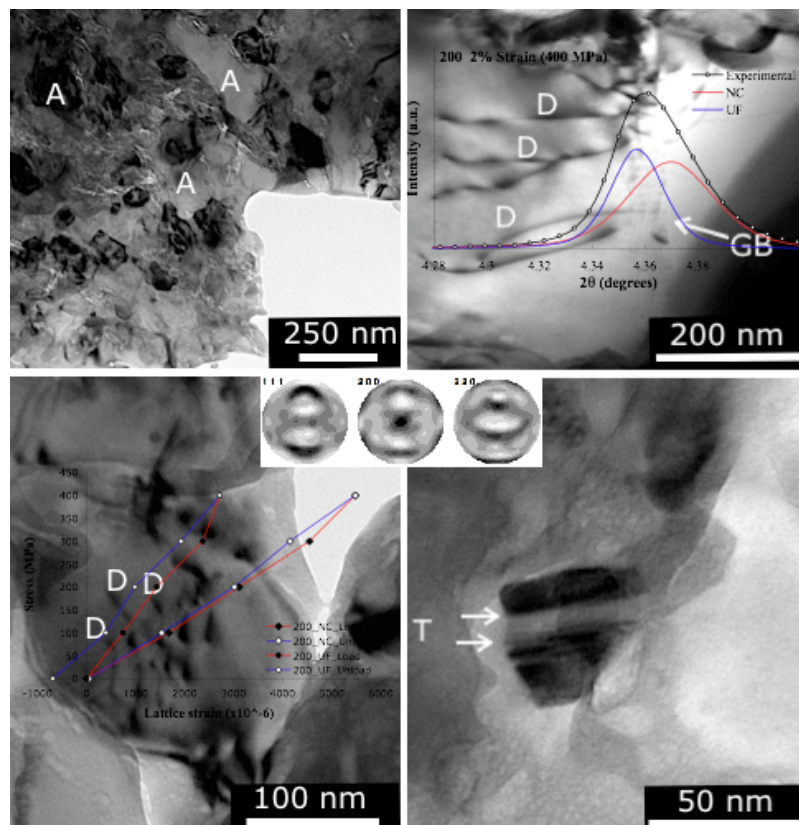
UNIVERSITY  
OF TRENTO - Italy

Department of Materials Engineering  
and Industrial Technologies

Doctoral School in Materials Engineering – XXII cycle

## Deformation mechanisms in bulk nanostructured aluminum obtained after cryomilling and consolidation by spark plasma sintering

Ivan Lonardelli



30<sup>th</sup> April 2010

**Deformation mechanisms in bulk nanostructured aluminum obtained after cryomilling and consolidation by spark plasma sintering**

**Ivan Lonardelli**

Tutor:

Prof. Alberto Molinari

Doctoral Committee:

Prof. Paolo Scardi - Università degli Studi di Trento, Italy

Prof. Gernot Kosterz - ETH Eidgenössische Technische Hochschule,  
Switzerland

Prof. Emmanuel Garnier - Université de Poitiers, France

Date of dissertation: 30<sup>th</sup> April 2010

## Index

Introduction . . . . .	5
References . . . . .	7
1. Structural evolution of Al powder . . . . .	9
Mechanical milling . . . . .	9
Experimental . . . . .	10
<i>Cryogenic mill</i> . . . . .	10
<i>Powder characterization method</i> . . . . .	13
Results and discussion . . . . .	14
<i>Characterization of the as-milled powder.</i> . . . .	14
<i>Particle size distribution: characterization and study</i> <i>of the thermal stability</i> . . . . .	21
<i>Dislocation density and solute drag-driven thermal</i> <i>stability</i> . . . . .	27
Summary . . . . .	32
References . . . . .	33
2. Consolidation of cryomilled Al using spark plasma sintering	36
Introduction . . . . .	36
Experimental . . . . .	38
Results and discussion . . . . .	40
<i>Densification</i> . . . . .	40
<i>Microstructural characterization</i> . . . . .	46
Summary . . . . .	51
References . . . . .	52

3. Deformation mechanism and plastic strain recovery in	
bulk bimodal nc-UF aluminum . . . . .	54
Introduction . . . . .	55
Experimental procedure . . . . .	59
<i>Compression experiments.</i> . . . .	59
<i>In-situ synchrotron X-ray and neutron diffraction experiments</i>	
. . . . .	61
Data analysis . . . . .	66
<i>Rietveld method</i> . . . . .	66
<i>Lattice strain determination</i> . . . . .	67
<i>Microstructural determination</i> . . . . .	69
<i>Quantitative texture analysis</i> . . . . .	70
Results and discussion . . . . .	75
<i>Macroscopic stress-strain response</i> . . . . .	75
<i>In-situ synchrotron and neutron diffraction experiments:</i>	
<i>explaining the plastic strain recovery</i> . . . . .	88
Summary . . . . .	103
References . . . . .	104
Conclusions . . . . .	108
Publications . . . . .	111

## **Introduction**

Conventional engineering materials are usually polycrystalline solids where the average grain size is of the order of many micrometers. The recent advent of nanocrystalline (nc) materials (crystallite size <100-150 nm) has opened new opportunities for research and applications, and in the field of the "upper nano" (30 to 150 nm), research on mechanical properties has been focused to increase strength and ductility [1]. However, the increasing yield stress on decreasing grain size, is coupled to a low ductility because of the poor strain hardenability due to particular deformation mechanisms involved in nanostructured materials. Particularly, in the last decade significant efforts have been undertaken to determine whether nanocrystalline metals deform by dislocation interaction or by alternative mechanisms often predicted by atomistic simulations (deformation twinning, grain boundary sliding and rotation, and diffusion related phenomena) [2-4]. Recently, important observations in thin films of electrodeposited nc-Al and nc-Au [5] have shown that plastic deformation in these films is partially recoverable. These macroscopic observations follow the work of Budrovich and co-workers [6] in which a thin film of nc-Ni was analyzed during deformation using X-ray diffraction. They found a complete recovery of the peak broadening after loading-unloading tests, while no comparable recovery was observed for conventional coarse-grained face-centered cubic (fcc) metals.

All these very exciting studies were focused on thin film samples but there is no experimental evidence that confirms this "super-elastic" effect in bulk nanocrystalline metals.

Following the papers published a few years ago by Budrovic et al. [6] and Rajagopalan et al. [5], the fundamental goal of this PhD Thesis is to study the recovery of plastic deformation in bulk fine-grained Al samples

using in-situ high-energy synchrotron X-ray diffraction, along with complementary ex situ deformation study.

The work is basically organized in three main chapters. The first chapter reports a methodology to obtain, using a "top-down" approach, nanostructured Al powder, starting from commercially pure Al powder. It is well known that nanostructured Al powder can be produced by cryomilling [7]. However, several aspects, such as the role of liquid nitrogen during milling, the evolution of the microstructure, the thermal stability and so on, must be studied in order to have an insight of the kinetics of the milling. In general, the thermal (meta-)stability of a microstructure will depend on the lattice defects stored within and between grains and on the particles (oxides and nitrides) due either to a dispersion or a precipitation of a second phase from a solid solution. Particularly, for nanocrystalline materials, impurities segregated at the grain boundaries, nano-porosity and nano-particles either "pinned" at the grain boundaries must be considered as strong stabilizers for the nanostructure. In the case of aluminum milled in liquid nitrogen it was shown dispersoids adjacent to the grain boundaries [8] that act as obstacles to grain boundary motion [9, 10]. These particles provide a pinning force that would not be present in the mechanically milled Fe powder [11,12]. The proposed study of the thermal stability of nanostructured Al powder obtained after cryomilling process (Chapter 1) provides useful information that helps to optimize the subsequent sintering and consolidation process. In this line, good thermal stability of the powder coupled with a sintering technology capable to sinter materials in a short cycle time is of fundamental importance to realize bulk nanostructured materials. Spark plasma sintering (SPS) (also called pulsed electric current sintering), described in chapter 2, is a relatively new methodology in which pressure and temperature are applied simultaneously. For aluminum, both the powder and the die are

conductive and both are heated up by the Joule effect; moreover the powder is heated by contact with the die. The assumption is that high pulsed current density ( $10^7$  A m<sup>-2</sup>; 10 V) might generate localized microplasmas between particles [13]. This phenomenon can contribute to clean the particle surface, to break the oxide layer and to enhance the mass transport between particles, resulting in a short sintering time. With this technology, bulk bimodal nanostructured/ultrafine Al samples were obtained and characterized using TEM and X-ray diffraction techniques. The specimens obtained as described above, are used to investigate the plastic deformation behavior of bulk nanocrystalline-ultrafine Al under in situ compressive loading. This fundamental part of this work is presented in chapter 3. The interaction between a nanostructured matrix and ultrafine grains is presented using the macroscopic stress-strain response and a micromechanics approach in which lattice strain and texture analysis are characterized to justify the plastic strain recovery observed.

## References

- [1] Y. M. Wang, M. Chen, F. Zhou, E. Ma, *Nature* 419 (2002) 912.
- [2] M. Chen, E. Ma, K.J. Hemker, H. Sheng, Y. Wang, X. Cheng, *Science* 300 (2003) 1275.
- [3] H. Van Swygenhoven, *Science* 296 (2002) 66.
- [4] V. Yamakov, D. Wolf, S.E. Phillpot, A.K. Mukherjee, H. Gleiter, *Nat. Mater.* 1 (2002) 1.
- [5] J. Rajagopalan, J.M. Han, M.T.A. Saif, *Science* 315 (2007) 1831.
- [6] Z. Budrovich, H. Van Swygenhoven, P.M. Derlet, S. Van Petegem, B. Schmitt, *Science* 304 (2004) 273.
- [7] D.B. Witkin, E.J. Lavernia, *Progress in Mater. Sci.* 51 (2006) 1.

- [8] R. W. Hayes, P.B. Berton, R.S. Mishra, *Metall Mater Trans A* 35 (2004) 3855.
- [9] L.S. Shvindlerman, G. Gottstein, *Z Metallk* 95 (2004) 239.
- [10] V.Y. Novikov, *Scripta Mater* 55 (2006) 243.
- [11] T.R. Malow, C.C. Koch, *Acta Mater* 45 (1997) 2177.
- [12] F. Zhou, J. Lee, S. Dallek, E.J. Lavernia, *J. Mater Res* 16 (2001) 3451.
- [13] M Tokita, *Mater. Sci. Forum* 308-311 (1999) 83.

## **1. Structural evolution of Al powder**

### **Mechanical milling**

The initial goal of the ball milling was a development of dispersion-strengthened alloys in which the improvement of creep resistance was obtained by mechanical alloying of metallic and non-metallic constituents [1]. Following this philosophy, cryomilling was developed in order to reach the finest particle sizes in shorter milling times with smaller grain size when compared with mechanical alloying performed in air or in inert atmosphere (Ar) [2]. In the case of aluminum, mechanical alloying by use of room temperature (RT) ball milling was aided by the addition of an organic process control agent (PCA), which was necessary in order to prevent the welding of the particles [3]. One of the main problem of the f.c.c. metals during milling is the necessity to add methanol, stearic acid and/or paraffin compounds to prevent the formation of millimeter-sized agglomerates. Unfortunately, this means adding carbon and oxygen, and the integrity of the material is definitely lost. On the other hand, the addition of secondary particles might be necessary if we want to build an engineering material with enhanced mechanical properties and a good creep resistance. Nevertheless, there is the possibility to increase the strength of the material not only working on the formation of secondary-phase particles but also refining the microstructure in terms of grain size. In these terms, the possible advantages to using a cryogenic liquid, usually nitrogen, rather than carrying out the milling at room temperature, are that the low temperature suppresses the annihilation of dislocations and a larger dislocation density means that the nanostructure is obtained in a shorter time [4]. For softer metals like aluminum, the particular advantage of

the cryogenic temperature is that prevents substantial cold welding and agglomeration of the powder during milling even without using any PCA.

## **Experimental**

### *Cryogenic mill*

The cryomilling, nanostructuring and mechanical milling process at cryogenic temperatures, has attracted much interest and in the last decade methodologies and various milling machines were developed [5]. The cryomilling apparatus reported extensively in the literature consists of a Szegvari attritor mill that is modified to admit continuous flow of liquid nitrogen into the mill. The Szegvari attritor is one of the most widely used milling machines and this is due to the simplicity of the equipment itself and the ease of operation. The milling apparatus includes thermocouples to monitor the attritor and ensure that a constant level of liquid nitrogen and thus a constant milling environment is maintained. The liquid nitrogen flows into the vessel continuously and the evaporated nitrogen is exhausted through an aperture in which a filter is positioned to trap the powder possibly present in the gas flow. The mechanism and all the technical specifications are well described in the literature available from the Union Process, Inc. [6]. Fig1 a, reports the Szegvari attritor principle and Fig1 b, shows the modified Union Process apparatus used in this work.

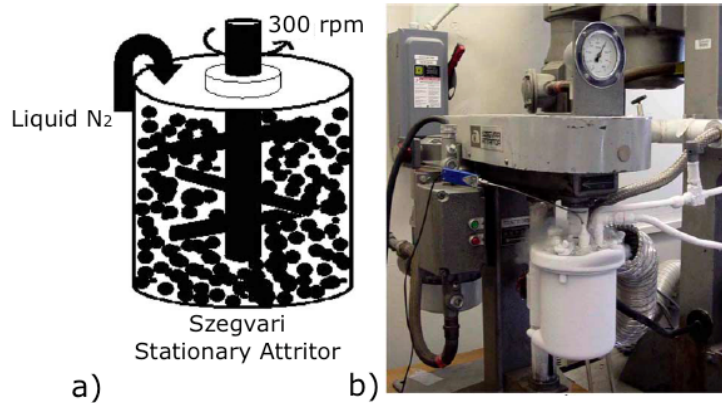


**Fig 1.** (a) Szegvari stationary attritor principle: the powder is deformed in liquid nitrogen by compression, friction and shearing due to several collisions and rub of balls. (b) Picture showing the cryomilling machine.

There are several advantages to use cryomilling:

- 1) Metal powder can be fractured and the microstructure reaches the nanometric scale (10 to 100 nm) limiting the formation of cold welding between particles.
- 2) The contamination from liquid nitrogen, which is considered a disadvantage of cryomilling, sometimes benefits the mechanical properties and thermal stability of the cryomilled materials as we will see later in this study.
- 3) The results are shown to be reproducible from one batch to another and the process may be scaled up from the laboratory to commercial production [6].

In this work, nanocrystalline aluminum (nc-Al) was produced by mechanical milling of a slurry of aluminum powders and liquid nitrogen using a modified Szegvari attritor (Union Process) as explained above. Elemental powder of commercially pure aluminum (particle size ranging from 45 to 200 micrometers) was used as raw material. The cryomilling process was performed with a stainless steel vial at 300 rotations per

minute (rpm) using stainless steel balls (6.4 mm diameter) with a ball to powder mass ratio of 32:1. Although this study is not focused on the optimization of the milling parameters, we have chosen the ideal rotational speed on the basis of recent work that has determined a range in which we can minimize both the milling time and the nitrogen lost [7]. Particularly, Fig 2 [7] shows the variation of the total cost of the cryomilled powders calculated taking into account the effect of milling time and the effect of nitrogen consumption. Based on these two factors, the total cost is low and relatively constant, between 300 and 600 rpm.

During the milling operations, the stainless steel vial (1.4 liters capacity) was filled with liquid nitrogen to maintain complete immersion of the milling media. Liquid nitrogen was used also as lubricant without any process control agent (PCA) added.

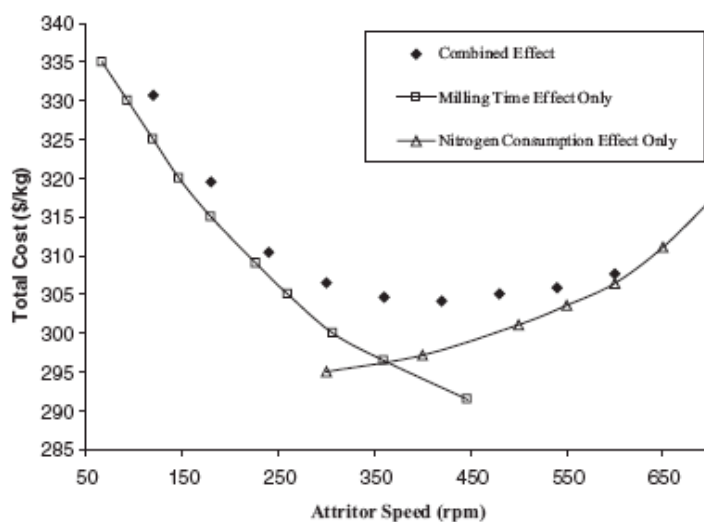


**Fig 2.** Total cost of cryomilled Al/B<sub>4</sub>C as a function of the attritor speed. Cost data are based on laboratory scale processing [7].

### Powder characterization method

Both the starting and cryomilled powders were sieved to determine the particle size distribution before and after the milling process.

At different steps of the milling process the Al powder was characterized using X-ray diffraction (XRD) to follow the grain refinement. After 25 h of milling, each granulometric fraction obtained from the sieving was analyzed by XRD before and after the heat treatments in high vacuum ( $10^{-5}$ ) at three different temperatures (350°C, 450°C and 550°C). The heat treatments were carried out in a Tersid tubular oven.

Each diffraction pattern was collected using a laboratory diffractometer operating with a Cu  $\alpha$  ( $\lambda=1.5418 \text{ \AA}$ ) source and an image plate detector over the  $2\theta$  range from  $10^\circ$  to  $100^\circ$  in reflection geometry (Fig 3). The X-ray sensitive imaging plates were exposed for 2 h and then acquired with the Perkin-Elmer "Cyclone" system.

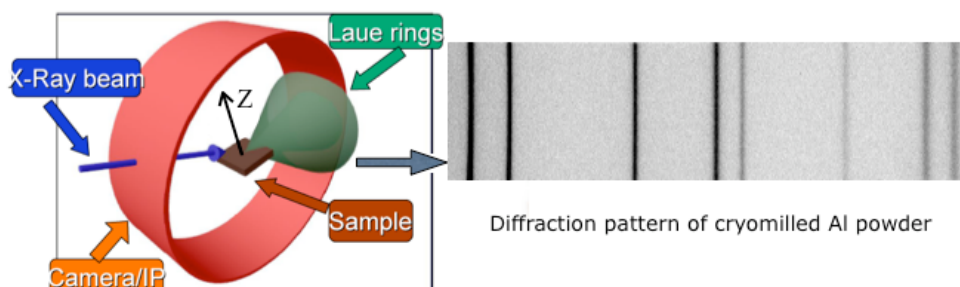


**Fig 3.** Diffraction setup used in the experiments. Diffraction in Bragg (reflection) geometry were collected using a phosphor imaging plate. On the right an example of the diffraction pattern for cryomilled Al collected using the image plate.

The analyses were performed using MAUD (Materials Analysis Using Diffraction) software [8], a Rietveld code [9] written in Java.

Instrumental broadening was determined using silicon as standard reference material (NIST 640c). "Delf" and "Distribution" were used as line broadening models, considering an isotropic model to describe the shape of the size-strain. "Delf" is similar to an integral breadth method and is described in [10, 11]. "Distribution" is actually the Warren-Averbach reversed and this size model is described in [12].

Transmission electron microscopy (TEM) observations were performed on the cryomilled powder using a Philips CM12 microscope operating at 120 kV to investigate the microstructure reached after 25 hours of milling.

Differential scanning calorimetry (DSC) using a Netzsch STA 409 Luxx apparatus was performed for each granulometric fraction to underline some differences regarding the exothermic peak corresponding to the grain growth (lost of the thermal stability). In all cases a protective atmosphere was used (Ar/5%H<sub>2</sub>) to prevent oxidation phenomena. The heating was performed at 20 K/min up to 650°C.

## **Results and Discussion**

### *Characterization of the as-milled powder*

As mentioned above, in order to evaluate the evolution of the microstructural refinement during the top-down approach at cryogenic temperature, X-ray diffraction method has been used. A small quantity of powder was picked up at different milling time and crystallite size and microstrain were determined from XRD using the Rietveld method. Fig 4 shows the evolution of the mean crystallite size and microstrain as a function of milling time.

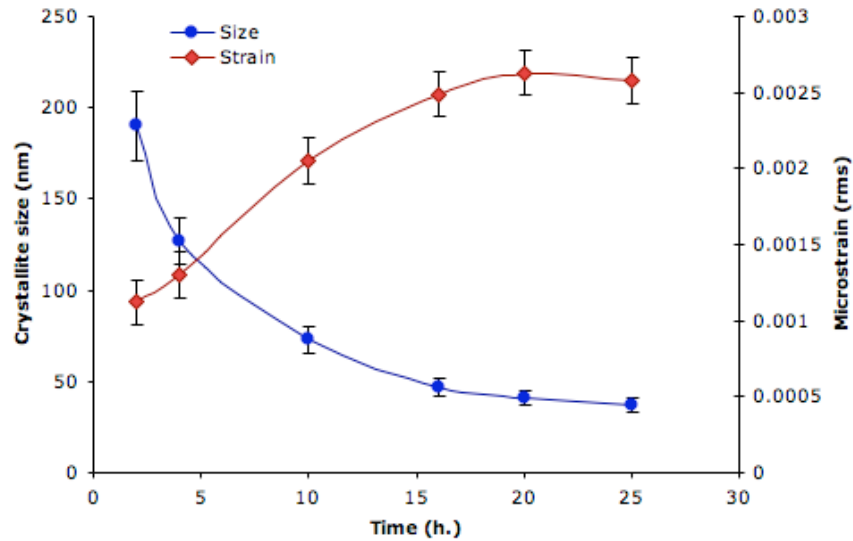


**Fig 4.** The mean crystallite size and the microstrain (defined as “root of means square”) as a function of the milling time.

As the milling proceeds, the density of defects increases resulting in an increasing of microstrain. It should be noted that the increase of the microstrain is followed by a slight decrease once the grain refinements takes place.

This behavior indicates that the dislocations tend to arrange each others into dipoles minimizing the energy of their strain field [13-15]. This arrangement of dislocations can be associated with the formation of dislocation walls resulting in the decrease of the apparent crystallite size [16]. The development of the nanostructure can be described as suggested by Fecht [17] in which a three-stage process was proposed (Fig 5).

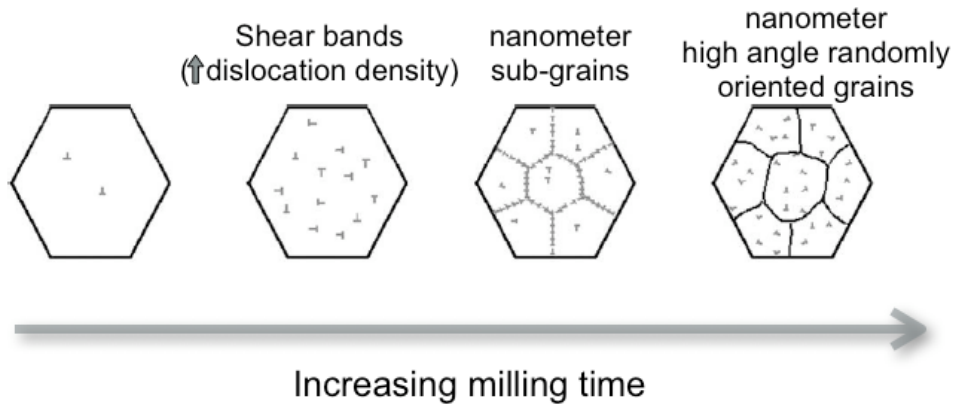


**Fig 5.** Schematic representation of the grain refinement during the milling process.

First, during the initial stage of deformation, there is an increase of dislocation density. A second stage is characterized by annihilation and recombination of dislocations, forming nanometer scale of sub-grains. Finally there is the transformation of sub-grains in randomly oriented high-angle grain boundaries. Fig 6 a and b show a bright field (BF) and a dark field (DF) TEM images (insert is the selected area electron diffraction (SAED) pattern) of the cryomilled powder in which some nanometric grains are clearly visible.

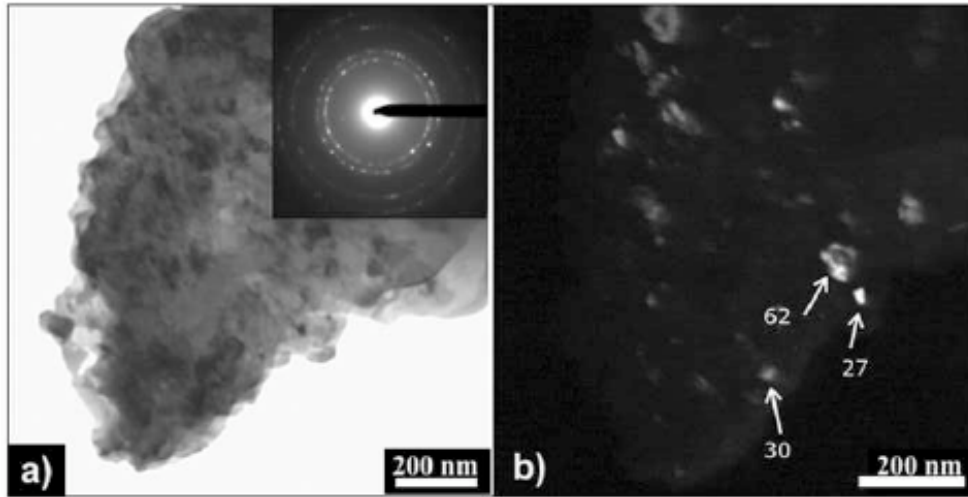


**Fig 6.** TEM images of Al powder after milling (25h) in liquid nitrogen. Bright field (a) and dark field (b) show nanometric grains. The grain size is broad distributed (see dark field picture) ranging between 27 and 62 nm.

We observe a broad distribution of the grain size (here in Fig 6 the size varies between 27 and 62 nm) where only few grains approach the minimum grain size that is obtainable by milling as suggested by Koch and Eckert [18, 19]. Particularly, the minimum value of the crystallite size that can be reached by ball milling depends to the intrinsic properties of the material (crystal structure) as suggested by theoretical and experimental studies cited above. A general empirical relationship for fcc, bcc and hcp systems can be represented as follows:

$$\frac{d_{\min}}{b} = A \exp[-cT_m]$$

where,  $b$  is the magnitude of the Burgers vector,  $T_m$  is the melting temperature and  $A$  and  $c$  are constants.

A recent dislocation model that supports this empirical equation, was proposed by Mohamed and co-workers [20] in which the minimum grain size is governed by a balance between the hardening rate introduced by dislocation generation and the recovery rate arising from dislocation annihilation and recombination. The model suggests proportionality between the minimum grain size and stacking fault energy and an exponential dependence with the activation energy for recovery. For pure aluminum, the minimum crystallite size attainable by ball milling is around 22 nm [20], and is not expected to further decrease by cryomilling. This is reasonably due to the high stacking fault energy and low activation energy for the recovery of dislocations in this metal.

As a confirmation, Zhou and co-workers [21, 22] report a mean crystallite size of 26 nm on a cryomilled Al powder, and an isotropic microstrain of 0.15% similar to that reported by Eckert and co-workers on a ball milled Al powder.

The minimum crystallite size obtained here (37 nm) is significantly larger suggesting that nanostructuring process has not been completed. Fig 7 shows the inverse correlation between the crystallite size and microstrain.

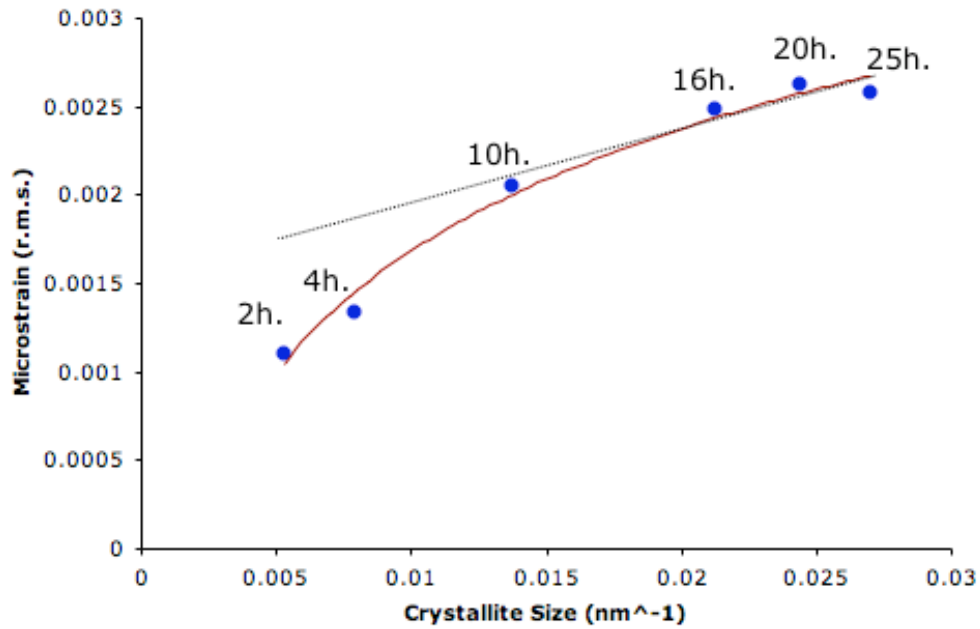


**Fig 7.** Microstrain vs. the reciprocal of crystallite size for the measured powder during milling.

Tian and Atzon [23] carried out low energy milling experiments on pure iron, under different vibration amplitudes and milling. They found a linear relationship between  $\langle \varepsilon^2 \rangle^{1/2}$  (where  $\varepsilon$  is the local strain) and  $d^{-1}$  in a size range below 40 nm.

Here the linear behavior is almost reached for a grain size less than 73 nm. The loss of linearity for points that are representative of the larger crystallite size might be ascribed to the poor sensitivity of the laboratory diffractometer in measuring crystallites when they are approaching 150 nm.

So far, we have described the evolution of the Al powder during milling. We can summarize the results as follow:

- 1) Using the cryomilling process without any PCA, the aluminum powder reached the nanostructure after 16 hours. The mean crystallite size after 25 hours was 37 nm.
- 2) Both the crystallite size and microstrain plots show a sort of lower and upper limit respectively. An approximately linear relationship between the inverse of the crystallite size and the microstrain is confirmed below 73 nm
- 3) After 25 h of milling at cryogenic temperature, the mean crystallite size does not reach the expected minimum value (22 nm) and the size is broad distributed, as confirmed by TEM investigation.

It should be pointed out that for the starting Al powder, the particle size distribution is broad and the milling process cannot be “homogeneous”. The consequence is a different behavior during milling; some particles start to refine the microstructure early but some others, later. At the end of the process, after the same milling time we have still a distribution of particle sizes as shown in Fig 8.

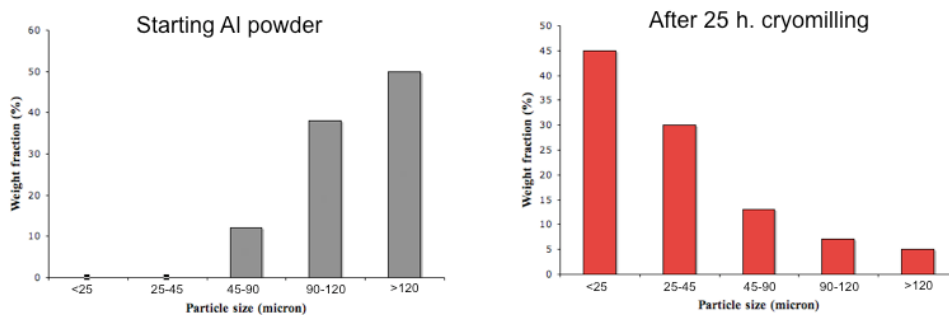


**Fig 8.** Particle size distribution (sieving), before and after cryomilling.

We might expect that the difference in particle size can reflect also a significant change in the microstructure, leading to a strong variation in the behavior during the consolidation process.

For this reason the next paragraph will be focused on the study of the microstructure and its thermal stability as a function of the particle size, considering the same milling time.

*Particle size distribution: characterization and study of the thermal stability*

Here, we present results of microstructural investigation and the thermal stability of nanostructured aluminum powder obtained after the cryomilling process considering five different granulometric classes.

It should be noted that, both the particle size and the crystallite size achieved by milling are broadly distributed. Fig 9 summarizes at different levels the dimensional changes in the Al powder, after 25 hours of cryomilling.

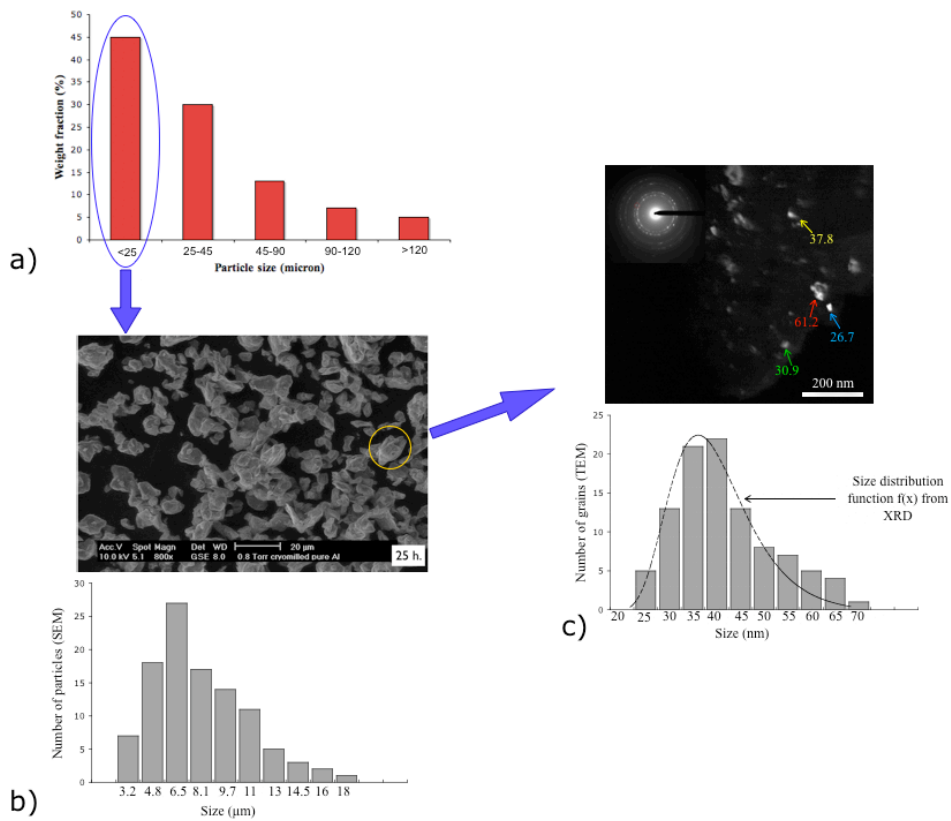


**Fig 9.** (a) Particle size distribution of Al powder after 25 hours of cryomilling.(b) Scanning electron microscopy (SEM) shows a broad distribution of the finer fraction ( $< 25 \mu\text{m}$ ). (c) TEM DF image reveals a broad distribution of the grain size. TEM distribution obtained using several DF images is compared with the X-ray distribution function.

The presence of a broad distribution of the particle size means that a consistent volume fraction of the powder did not complete the refinement process (high angle grain boundary formation and thus fragmentation).

This is important since the control of the grain size distribution during consolidation processes is of paramount importance to achieve the desired mechanical properties of a nanocrystalline material.

Average crystallite size and microstrain (%) for each granulometric class (Fig 9a) were determined using XRD. The results and some experimental diffraction patterns are reported in Fig 10. The broader are the peaks, the smaller the particles, resulting in a larger microstrain.

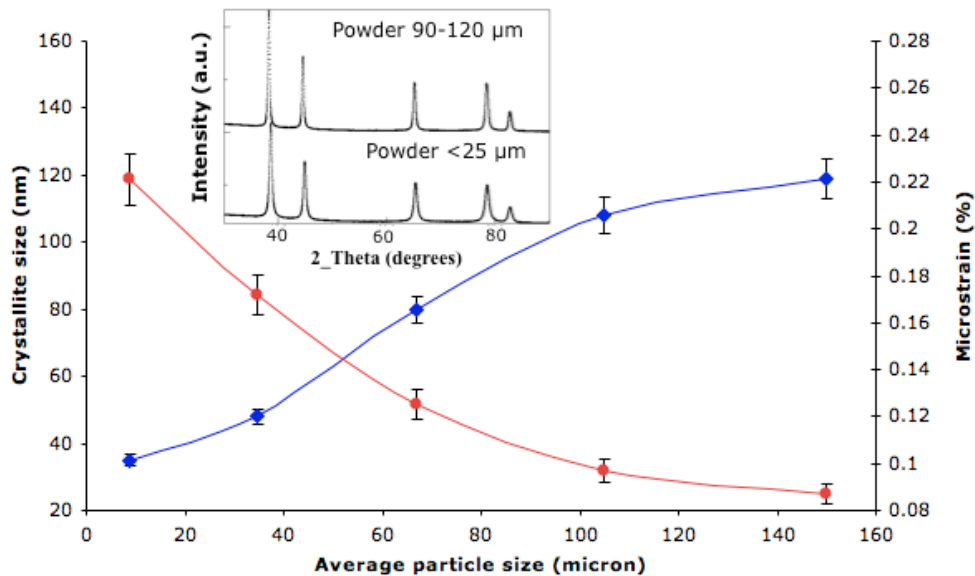


**Fig 10.** Crystallite size and microstrain changes as a function of the mean particle size for the five granulometric fractions. Insert picture shows the diffraction patterns of the milled powder (25 h) for two different granulometric classes. Note the difference of the peak broadening.

Table 1 summarizes the results from XRD line profile analysis performed on the five granulometric fractions and reported in Fig 10.

Table 1. Crystallite size  $d$  and microstrain  $\langle \varepsilon^2 \rangle^{1/2}$  of the five granulometric fractions. The values of standard deviation are from the Rietveld refinement.

Granulometric class ( $\mu\text{m}$ )	$d$ (nm)	$\langle \varepsilon^2 \rangle^{1/2}$ (%)
<25	35 (1)	0.221 (10)
25-45	48 (2)	0.172 (11)
45-90	80 (3)	0.125 (13)
90-120	108 (6)	0.097 (11)
>120	119 (6)	0.087 (12)

The behavior of the five different granulometric classes investigated after 25 h of cryomilling (in terms of crystallite size and microstrain changes) is very similar to what is reported in Fig 4 and 7 considering different milling times.

Fig 11 shows the mean crystallite size versus annealing temperature (1 h. holding) for each granulometric fraction. The grain growth tendency is quite different, and increases with increasing the starting grain size.

A brief description can be given as follows:

- A grain size of 35 nm is stable up to 350°C, then it slightly increases, but remains nanocrystalline over the whole temperature range investigated (78 nm at 550°C)
- Powder of a grain size of 48 nm has the same behavior and still remains nanocrystalline (155 nm at 550°C)
- Powder of grain sizes of the 80 nm, 108 nm and 119 nm behave differently, losing the nanostructure between 350°C and 450°C.

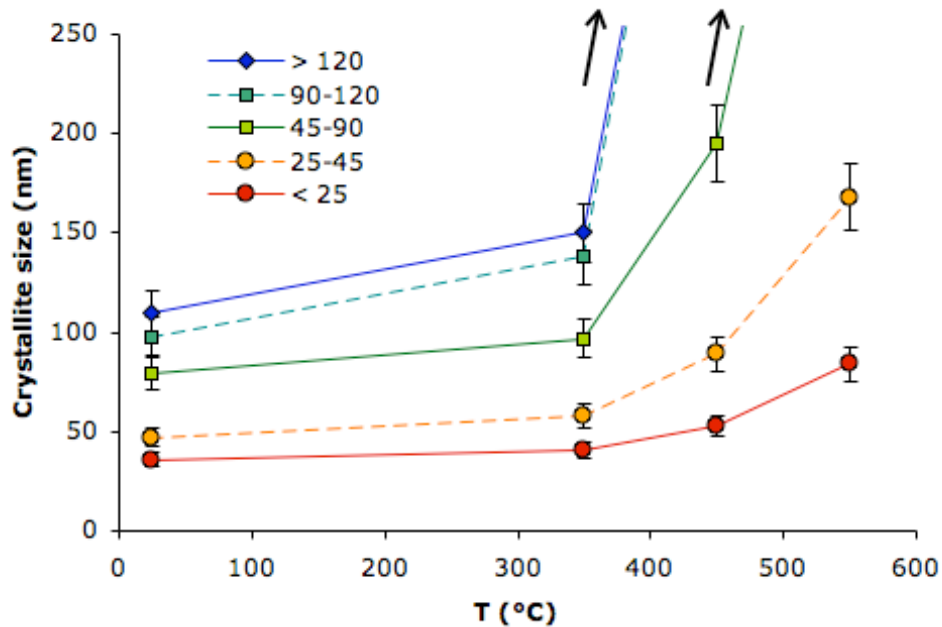


**Fig 11.** Grain growth of the five granulometric classes. For each temperature considered (350°C, 450°C, 550°C) isothermal heat treatments in high vacuum (1h,  $10^{-5}$ ) were performed. The arrows indicate that for higher temperatures the crystallite size is actually not detectable with XRD laboratory technique.

Grain growth of 26 nm aluminum has been investigated by Zhou and co-workers [22]. They found that growth is very limited up to 450°C, without any appreciable effect of the holding time; above this temperature, substantial time-dependent grain growth occurs. This means that below 450°C grain boundary pinning forces are active, resulting in a temporal exponent of grain growth lower than 0.5.

Zhou and co-workers conclude that nanostructured Al is stable up to homologous temperatures as high as 0.78, because of the effect of the solute drag, pore drag, second particles drag. Among the powders investigated here only the two most finely grained follow the trend

reported by Zhou. The results of Fig. 11 show that the resistance to grain growth decreases with increasing the initial grain size. This behavior shows a tendency to growth that is less pronounced in the finer microstructure, in contrast to the driving force of the grain growth that tends to minimize the grain boundary area.

Fig 12 shows the DSC curves that describe a qualitative characterization of the energy release during grain growth for each different granulometric fractions (coarse particles  $>120\ \mu\text{m}$  are not considered).

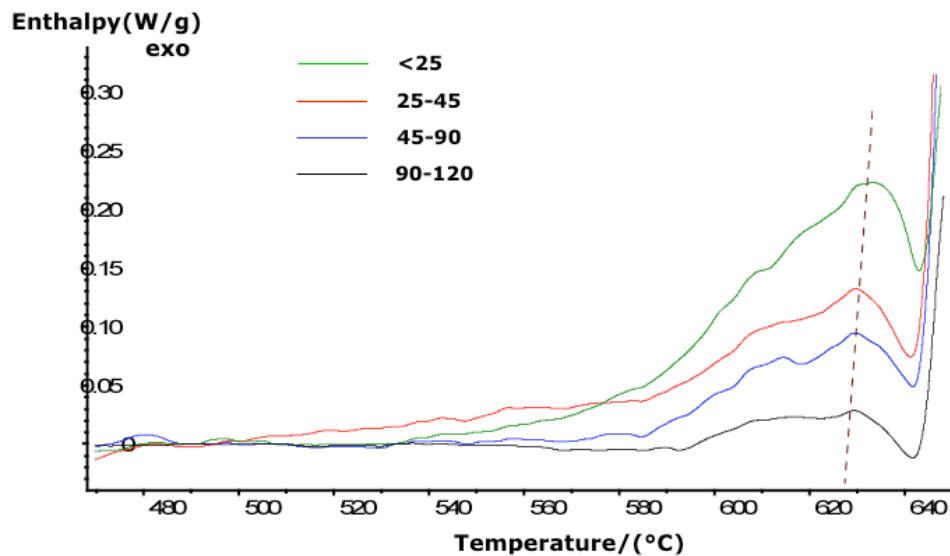


**Fig 12.** Enthalpy release describes the grain growth as a function of the particle size. The heating rate used was 20K/min.

The grain growth is a thermally activated process. For this reason the peak position indicating the onset of grain growth is influenced by the heating rate. In this case, the heating rate is constant for each

measurement, so the peak shift is ascribed to a sort of “opposing force” that stabilizes the grain size.

Here, the finer powder (<25 micrometer with an average grain size of 35 nm) displays the grain growth peak at highest temperature even if the driving force is very high. In the next paragraph we try to give a possible interpretation of the thermal stability described above.

#### Dislocation density and solute drag-driven thermal stability

The driving force for the grain growth is the excess of Gibbs energy correlated to the grain boundary surface, and is expressed by the following equation

$$\Delta G = \gamma_{gb} \Delta S = 3.3\gamma_{gb} / d$$

where  $\Delta S$  is the specific grain boundary surface,  $D$  is the crystallite diameter and  $\gamma_{gb}$  is the specific grain boundary energy [24]. If  $\Delta G$  increases with decreasing mean crystallite size then, from a thermodynamic point of view, the smaller the grain size, the larger the tendency to grain growth. Grain growth at homologous temperatures below 0.5 is however opposed by lattice defects (dislocations, stacking faults etc.) that interact with each other. In this study, the average microstrain and domain size determined by XRD (Table 1) were transformed to a dislocation density as described by Mukherjee et al. [25]. The average density of dislocation ( $\rho$ ) has been estimated from the following equation:

$$\rho = (\rho_D \rho_S)^{1/2}.$$

Table 2 reports the resulting dislocation densities calculated for each granulometric class. The dislocation density ranges from  $0.8 \times 10^{14} \text{ m}^{-2}$  to  $7.35 \times 10^{14} \text{ m}^{-2}$ . These values are compatible to that of a highly deformed aluminum. As observed by Moelle and co-workers, the grain boundary mobility is reduced by large strain accumulated in the adjoining regions [20]. This implies that grains can grow only after a certain amount of strain has been released by recovery.

If a grain boundary is described as an array of dislocations, the resistance offered by strain accumulated between and within the grain can be expressed by the stress required to move the dislocations against. This approach was used by Chatterjee and co-workers [26] to study mechanical stabilization of austenite in martensitic transformation, and applied by Molinari and co-workers [27], to study thermal stability of nanostructured Fe-Mo alloy. From a micromechanic point of view, it may be assumed that the grain boundary motion is driven by the stress  $\tau_1$  resulting from the driving force of grain growth, and is opposed by the resistance  $\tau_2$ , the friction force induced by the dislocations in the strained regions.

The two stresses are given by the following two equations [26]:

$$\tau_1 = \Phi \Delta G = \Phi \gamma_{gb} \Delta S = 3.3 \Phi \gamma_{gb} / D$$

$$\tau_2 = Gb\rho^{1/2} / 8\pi(1 - \nu)$$

where  $\Phi$  is a constant, assumed to be equal to unity,  $\Delta G$  is the driving force for grain growth,  $\Delta S$  is the specific grain boundary surface entropy,  $d$  is the average crystallite diameter,  $G$  is the shear modulus,  $b$  is the modulus of the Burgers vector of dislocations,  $\rho$  is the dislocation density,  $\nu$  is the Poisson's ratio, and  $\gamma_{gb}$  is the specific grain boundary energy.

The equilibrium between the two stresses defines a critical dislocation density  $\rho_{cr}$ , which is given by the following equation:

$$\rho_{cr} = \gamma_{gb}^2 [26.4\pi(1-\nu)]^2 / D^2 G^2 b^2$$

If  $\rho < \rho_{cr}$  crystallites can grow. On the contrary, if the  $\rho > \rho_{cr}$  they cannot grow till the exceeding dislocation density has been removed.

The critical dislocation density was calculated, using two different values of the specific grain boundary energy: 0.18 J/m<sup>2</sup> and 0.32 J/m<sup>2</sup>. These two values were reported by Zhang and co-workers [28] as the extremes of  $\gamma_{gb}$ , in dependence on the mismatch angle between grains. Results are reported in Table 2 and compared with the dislocation density in the nanometric grains of the five granulometric fractions of the cryomilled powder.

Table 2. Crystallite size ( $d$ ), dislocation density ( $\rho$ ) and critical dislocation density ( $\rho_{cr}$ ) of the cryomilled powder calculated for each granulometric fraction, using two different values of the specific grain boundary energy [28].

Particle size ( $\mu\text{m}$ )	$d$ (nm)	$\rho$ (m <sup>-2</sup> )	$\rho_{cr}$ (m <sup>-2</sup> )	$\rho_{cr}$ (m <sup>-2</sup> )
<25	35 (1)	0.74x10 <sup>15</sup>	1.47x10 <sup>15</sup>	4.66x10 <sup>15</sup>
25-45	48 (2)	0.49x10 <sup>15</sup>	0.78x10 <sup>15</sup>	2.48x10 <sup>15</sup>
45-90	80 (3)	0.19x10 <sup>15</sup>	0.28x10 <sup>15</sup>	0.89x10 <sup>15</sup>
90-120	108 (6)	0.10x10 <sup>15</sup>	0.15x10 <sup>15</sup>	0.49x10 <sup>15</sup>
>120	119 (6)	0.08x10 <sup>15</sup>	0.13x10 <sup>15</sup>	0.40x10 <sup>15</sup>

Independent of the specific grain boundary energy considered, the critical dislocation density is higher than the actual dislocation density. It

might be concluded that the lattice strain is too low to stabilize the nanostructure, and consequently, crystallites could grow immediately when heated. However, other stabilizing mechanisms not correlated to the density of dislocation have to be active. The two stresses  $\tau_1$  and  $\tau_2$  were calculated for the five granulometric classes, and results are reported in Table 3.

Table 3. Calculated shear stresses acting on the GB of the milled powder

$\tau_1(\text{N/m}^2)$	$\tau_1(\text{N/m}^2)$	$\tau_2(\text{N/m}^2)$	$\tau_1 - \tau_2(\text{N/m}^2)$	$\tau_1 - \tau_2(\text{N/m}^2)$
$\gamma_{gb}=0.18$	$\gamma_{gb}=0.32$		$\gamma_{gb}=0.18$	$\gamma_{gb}=0.32$
$1.7 \times 10^7$	$3.0 \times 10^7$	$1.15 \times 10^7$	$0.55 \times 10^7$	$1.85 \times 10^7$
$1.2 \times 10^7$	$2.2 \times 10^7$	$0.94 \times 10^7$	$0.26 \times 10^7$	$1.26 \times 10^7$
$0.74 \times 10^7$	$1.3 \times 10^7$	$0.58 \times 10^7$	$0.16 \times 10^7$	$0.72 \times 10^7$
$0.55 \times 10^7$	$0.98 \times 10^7$	$0.42 \times 10^7$	$0.13 \times 10^7$	$0.56 \times 10^7$
$0.50 \times 10^7$	$0.89 \times 10^7$	$0.39 \times 10^7$	$0.11 \times 10^7$	$0.50 \times 10^7$

The values decrease with increasing crystallite size, but  $\tau_1$  is around one order of magnitude higher than  $\tau_2$ .

The difference between the two stresses, which is also reported in Table 3, is a measure of the forces opposing grain growth not related to the dislocation density. These forces can be summarized as follow:

- drag stress exerted by segregated impurities
- second-phase nanoparticles
- nanopores at the grain boundary

The value of the difference between  $\tau_1$  and  $\tau_2$  decreases with increasing the crystallite size, and confirms the results reported in Fig 11. The balance between stresses driving grain growth and stresses opposing it confirms that, from a micromechanics point of view, the smaller the

crystallite size the more stable the nanostructure on heating. As reported extensively in the literature [29-31], grain growth is strongly inhibited by the pinning effect due to the presence of second-phase particles. For the cryomilled aluminum powders it is reasonable to assume the formation of AlN or Al-oxynitride phases as a consequence of the milling process and/or subsequent annealing. In the case of cryomilling, the liquid nitrogen is in direct contact with the aluminum powder so, the most probable impurity is nitrogen. It might segregate at the grain boundary as solute clusters, and cause precipitation of AlN nanoparticles between and within Al grains upon heating. Since the contamination of the powder during milling comes from the interaction between the Al particles and the milling media, the finer the particle size, the more surface can interact with nitrogen.

Fig 13 shows the nitrogen content versus the force opposing grain growth. As expected, the quantity of nitrogen increases with decreasing the particle size. The nitrogen content measurements were performed after a degassing process, in which each granulometric fraction was heat treated at 350°C for 15 h in high vacuum ( $10^{-5}$  mbar).

However, the identification of second-phase particles or nanopores is very hard in the as-milled powder. To characterize in more detail the second-phase particles, the finer powder was consolidated at 620°C using spark plasma sintering (SPS), a process that will be described in the next chapter.

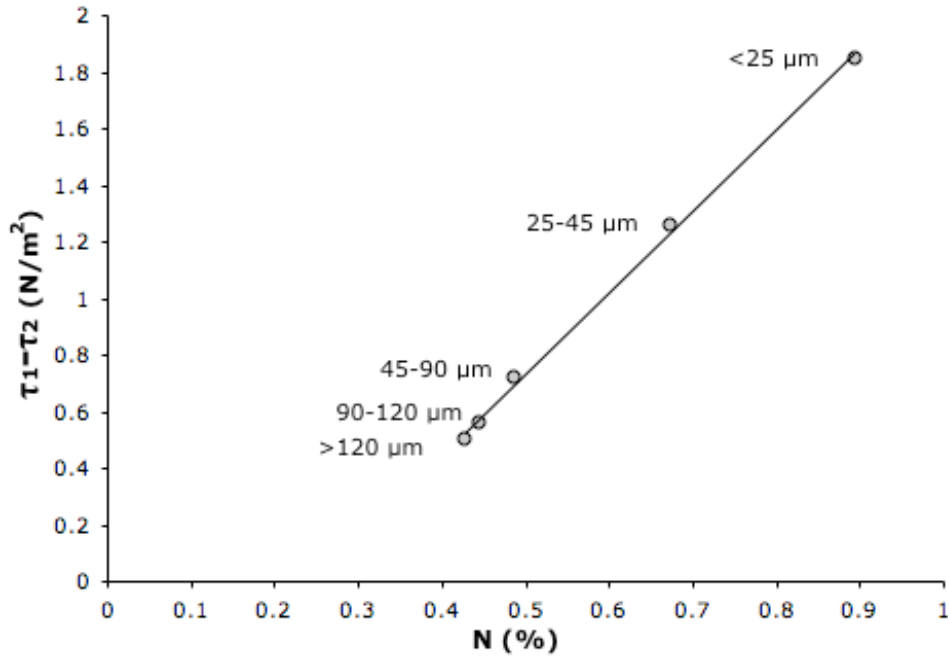


**Fig 13.** The force opposing grain growth due to the drag stress exerted by the second-phase particles and nanopores vs. nitrogen content (at. %) for each granulometric fraction, after degassing at 350°C.

### Summary

A nanostructured Al powder was obtained using cryogenic mechanical milling. The powder produced after 25 h. of milling in liquid nitrogen shows a quite broad distribution of the particle size, ranging from a few  $\mu\text{m}$  up to about 150  $\mu\text{m}$ . We have selected five different granulometric classes (<25  $\mu\text{m}$ , 25-45  $\mu\text{m}$ , 45-90  $\mu\text{m}$ , 90-120  $\mu\text{m}$  and >120  $\mu\text{m}$ ) and for each of these, structural and microstructural features, as well as the thermal stability were investigated using ex-situ X-ray diffraction and transmission electron microscopy. We found a direct correlation between particle size and crystallite size with an obvious increase of lattice defects with the fragmentation of the powder. The grain growth

tendency was found to depend strongly on the initial grain size (and thus particle size) with noticeable changes of the thermal stability for the five granulometric classes considered. Particularly the quantity of nitrogen content measured (after degassing) in each of the five granulometric classes increases with decreasing the particles/crystallite size. This might justify why the calculated drag stress exerted by segregated impurities, second phase particles and pores is effectively higher for small particles. In the next chapter the second phase particles and nanopores will be characterized in more detail using bulk consolidated samples and TEM techniques.

## References

- [1] P.S. Gilman, J. S. Benjamin, *Ann Rev Mater Sci* 13 (1983) 279.
- [2] M. J. Luton, C.S. Jayanth, M.M. Disko, S. Matras, J. Vallone, *Mater Res Soc Symp Proc* 132 (1989) 79.
- [3] M. Zadra, F. Casari, I. Lonardelli, G. Ischia, A. Molinari. *Intermetallics*, 15 (2007) 1650.
- [4] F. Zhou, X.Z. Lia, Y.T. Zhu, S. Dallek, E.J. Lavernia, *Acta Mater* 51 (2003) 2777.
- [5] C. Suryanarayana, *Prog. Mater. Sci.* 46 (2001) 1.
- [6] A. Szegvari, M. Yang, Attritor Grinding and Dispersing Equipment, company literature from <http://www.unionprocess.com/literature.html>
- [7] J Ye, J M Schoenung, *Adv. Eng. Mat* 6 (2004) 656.
- [8] L. Lutterotti, S. Matthies, H.R. Wenk, A.S. Schultz, J.W.Jr Richardson, *J. Appl. Phys.* 81 (1997) 594.
- [9] H.M. Rietveld, *J. Appl. Cryst.* 2 (1969) 65.
- [10] L. Lutterotti, P. Scardi, *J. Appl. Cryst.* 23 (1990) 246.

- [11] T. H. de Keijser, E.J. Mittemeijer, H.C.F. Rozendaal, *J. Appl. Cryst.* 16 (1983) 309.
- [12] N.C. Popa, D. Balzar, *J. Appl. Cryst.* 35 (2002) 338.
- [13] D. Fatay, E. Bastarash, K. Nyilas, S. Dobatkin, J. Gubicza, T. Ungar, *Z. Metallkunde* 94 (2003) 847.
- [14] J. Gubicza, G.y Krallics, I. Shiller, D. Malgin, *Mater. Sci. Forum* 473-474 (2004) 453.
- [15] J. Gubicza, N.H. Nam L. Balogh, R.J. Hellmig, V.V. Stolyarov, Y. Estrin, T. Ungar, *J. Alloys and Compounds* 378 (2004) 248.
- [16] T. Ungar, J. Gubicza, *Z. Kristallogr.* 222 (2007) 114.
- [17] H.J. Fecht, *Nanostruct Mater* 6 (1995) 33.
- [18] C.C. Koch, *Nanostruct Mater* 9 (1997) 13.
- [19] J. Eckert, J.C. Holzer, C.E. Krill III, W.L. Johnson, *J. Mater Res* 7 (1992) 1751.
- [20] F. A. Mohamed, *Acta Mater* 51 (2003) 4107.
- [21] F Zhou, D Witkin, SR Nutt, EJ Lavernia, *Mater Sci Eng A* 375-377 (2004) 917.
- [22] F Zhou, J Lee, S Dallek, EJ Lavernia, *J Mater Res* 16 (2001) 3451.
- [23] H H Tian and M Atzon, *Acta Metall Mater* 47 (4) (1999) 1255.
- [24] C H Moelle, HJ Fecht, *Nanostruct Mater* 6 (1995) 421.
- [25] P Mukherjee, A Sarkar, P Barat, SK Bandyopadhyay, P Sen, SK Chattopadhyay, P Chatterjee, SK Chatterjee, MK Mitra, *Acta Mater* 52 (2004) 5687.
- [26] S. Chatterjee, HS Wang, JR Yang and HKDH Bhadeshia, *Mater Sci Technol*, 6 (2006) 641.
- [27] A. Molinari, S. Libardi, M. Leoni, P. Scardi, *Acta Mater.* 58 (2010) 963.

- [28] H Zhang, M Upmanyu, DJ Srolovitz, *Acta Mater* 53 (2005) 79.
- [29] K Song, M Aindow, *Mater Sci Eng A* 479 (2008), 365.
- [30] C L De Castro, B S Mitchell, *Mater Sci Eng A* 396 (2005) 124.
- [31] EJ Lavernia, B Q Han, J M Schoenung, *Mater Sci Eng A* 493 (2008) 207.

## 2. Consolidation of cryomilled Al using spark plasma sintering

### Introduction

Spark plasma sintering (SPS) is a pressure-assisted high temperature sintering method in which a high-temperature plasma (spark plasma) is generated in the gaps between powder particles as a consequence of an electrical discharge at the beginning of ON-OFF pulse currents. The system consists of a SPS machine with a vertical single-axis pressurization mechanism, specially designed punch electrodes incorporating water cooler, a water-cooled vacuum chamber, a vacuum/air/argon-gas atmosphere control mechanism, a special DC-pulse sintering power generator, a cooling water control unit, a position measuring unit, a temperature measuring unit, an applied pressure display unit and some interlock safety units [1]. Fig 14 shows the inside of the water cooling chamber where the powder is placed.

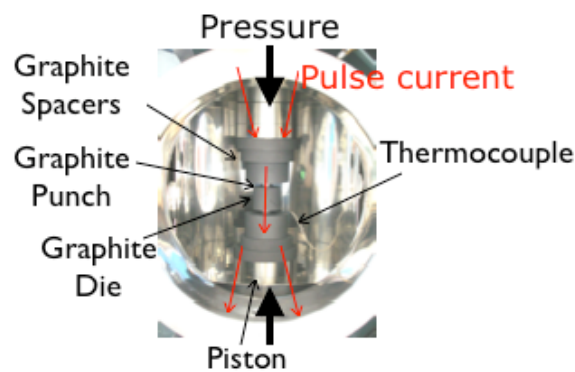


**Fig 14.** Sintering chamber (water cooled) in which the powder is placed in a graphite die (conductive material with excellent dimensional stability during the sintering process).

SPS systems offer many advantages over conventional systems using hot press (HP) sintering, hot isostatic pressing (HIP) or atmospheric furnaces. These advantages can be summarized as follows:

- easy sintering operation
- control of sintering energy
- high sintering speed
- low sintering temperatures
- high reproducibility

Particularly, SPS was designed to process materials that could not be sintered using conventional sintering methods and which suffer for a large thermal load. These materials are typically nanostructured metal powders, intermetallic powders and metal matrix composites (MMC) where, the powders are very hard and a first step of cold pressing (like in a conventional sintering process) becomes impracticable. Furthermore, the SPS mechanism suggests very short sintering times at lower temperatures. These advantages are crucial when we start with nanostructured metal powder and we want to obtain bulk samples that are still nanostructured, preventing abnormal grain growth. The advantages are reported with practical examples in literature [2-4].

Another advantage, is the possibility to generate current pulses of high current density (around  $10^7 \text{ A m}^{-2}$ ) that can form a local plasma into the gaps between the particles helping the consolidation. The SPS sintering process can be summarized in four steps as follow:

- 1) Generation of spark discharging by ON/OFF pulse energization.
- 2) Generation of sparks and plasma.
- 3) Vaporization and melting action on the particle surfaces.
- 4) Neck formation by spark plasma (thermal diffusion, particles migration and plastic deformations).

Fig 15 shows a representation of the pulsed current that flow through the conductive powder particles.

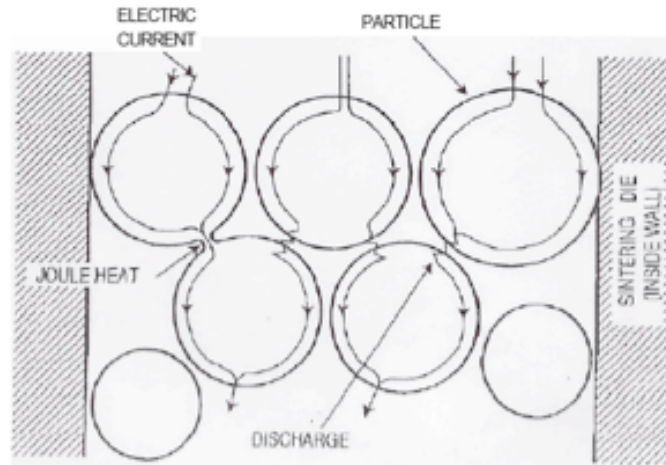


**Fig 15.** Pulsed current flow through conductive powder particles.

This plasma, although not verified, might play a fundamental role in the cleaning of the powder surface from contaminants and breaking the oxide layer that is inevitable formed after milling. Particularly, for pure aluminum it has been demonstrated that SPS really breaks the oxide layer, resulting in a sintering time of a few minutes at a temperature around 525-550°C [5, 6]. For these reasons the SPS consolidation process was chosen to produce full dense bulk nanostructured aluminum starting from cryomilled powders.

### **Experimental**

Nanostructured aluminum powder obtained after 25 h of cryomilling was used in the SPS consolidation process. It should be noted that, after milling, the cryomilled powder was immediately placed in a glove box filled with argon to prevent oxidation. Based on the thermal stability

study presented in chapter 1, the  $<25 \mu\text{m}$  powder and the  $25\text{-}45 \mu\text{m}$  powder were selected for the consolidation process.

Sintering was carried out in a DR.SINTER-1050 SPS system (Sumitomo Coal & Mining Ltd.) using a graphite die. Cylindrical specimens of 30 mm diameter and 10 mm height were sintered and machined with an electrical discharging machine (EDM) in order to obtain cylinders of 4.5 mm diameter and 10 mm thicker to perform compression tests (Chapter 3).

The die temperature was measured using a K type thermocouple inserted in it. However, the exact sample temperature was obtained after a correction, using previous results in which the temperature of an aluminum bulk sample and the die were monitored at the same time. In this work the sintering temperature refers to the real temperature at which the sample was produced.

Three different sintering temperatures were selected to produce bulk samples:  $550^\circ\text{C}$ ,  $600^\circ\text{C}$  and  $620^\circ\text{C}$ . A sintering schedule corresponding to  $T=600^\circ\text{C}$  (the others are similar) is reported in Fig 16.

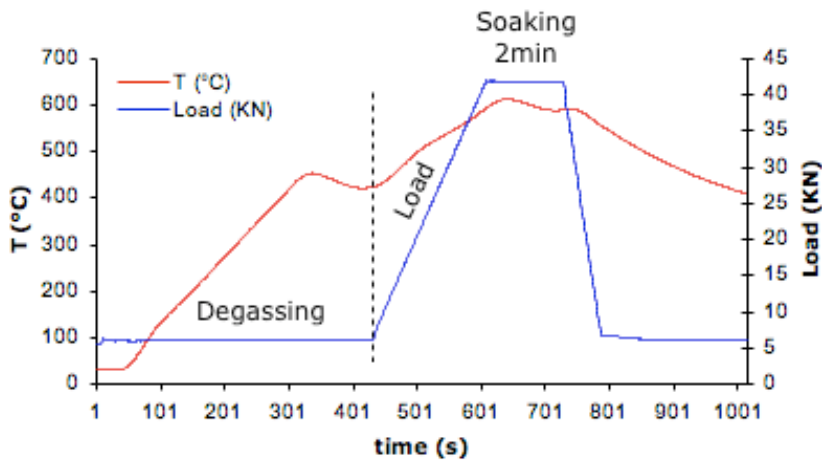


**Fig 16.** Temperature ( $^\circ\text{C}$ )-load conditions (kilonewton) applied during sintering.

The temperature was increased up to 400°C (heating rate of 100 K/min) and the load was maintained around 6 kN. At 400°C the load was increased to 43 kN (60 MPa) in 2 min and maintained till the end of the soaking time at 600°C (2 min). The densities of the three samples obtained at three different sintering temperatures were measured using Archimedes principle. Parts of sintered cylinders were used for metallographic inspection: they were cold mounted, ground and polished to 1 μm surface finish and then electrochemically etched with Barker's reagents.

The microstructure was characterized using TEM analysis. TEM examinations were carried out with a Philips CM 12 electron microscope operating at 120 kV. For the TEM analysis, the samples were mechanically thinned (80 μm thick), polished and subsequently ion milled.

XRD line profile analysis from synchrotron X-ray data (high-energy ID-1 beam line at APS, Chicago) was also used to characterize the microstructure.

## **Results and discussion**

### *Densification*

The as-sintered samples were measured by the Archimedes principle method in order to determine their relative densities. There is a significant increase of density with the sintering temperature. Figure 17 shows the values of the relative densities for the two granulometric fractions considered, as a function of SPS temperatures considered.

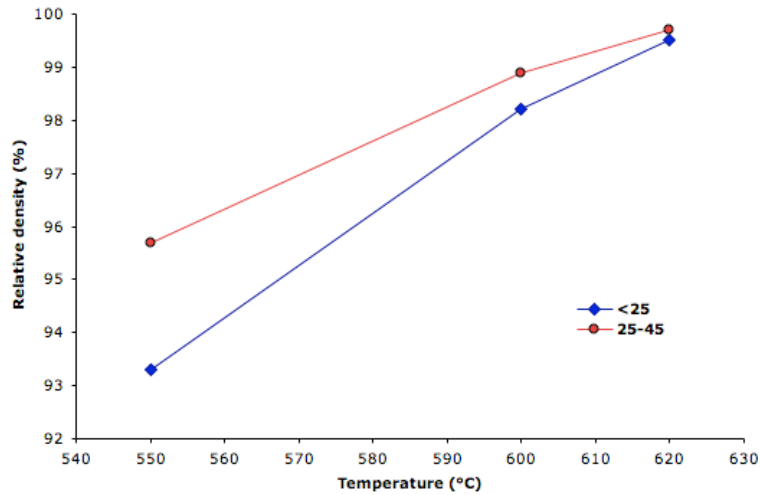


**Fig 17.** Relative densities of the cryomilled Al (<25  $\mu\text{m}$  ,blue line, and 25-45  $\mu\text{m}$  ,red line, are considered) compacts consolidates for 2 minutes under 60 MPa by SPS.

The relative density increases with increasing SPS temperatures and the particle size. This indicates that the smaller the particle size the higher the amount of nitrogen and oxygen absorbed on the surfaces of the particles, the more difficulties to reach the full density in the SPS consolidated samples. Moreover, the hardness of the powders increases with decreasing crystallite size (and then, from chapter 1 the particle size).

Fig 13 in the chapter 1 reports the force opposing grain growth as a function of the nitrogen content found in the five different granulometric fractions. Here the sintering process is influenced by two distinct phenomena:

- 1) the tendency of the nanometric grains to growth (the temperature)

2) the quantity of molecular nitrogen and oxygen trapped on the particles surfaces that is opposing to the compaction assisted by the pressure.

Owing to the upper limit of applied pressure using a graphite die (60 MPa max), only the SPS temperature was changed to reach the desired density and microstructure.

From Fig 4 we can conclude that the SPS sintering temperature has to be increased up to 620°C in order to activate the grain growth and reach a sufficient degree of compaction.

However, the effect of the applied pressure on the density, at a constant temperature, was recently studied [7, 8] and an evident increase of relative density with increasing pressure. On the other hand, these results imply that the die has to be made of material that is at the same time conductive, with a good dimensional stability during heating-cooling, and could sustain pressures on the order of 150-200 MPa. This is possible but very expensive and the philosophy of this work is to obtain bulk nanostructured Al samples at reasonable costs.

Fig 18a reports the dimensional contraction and its derivative as a function of time during the SPS consolidation process.

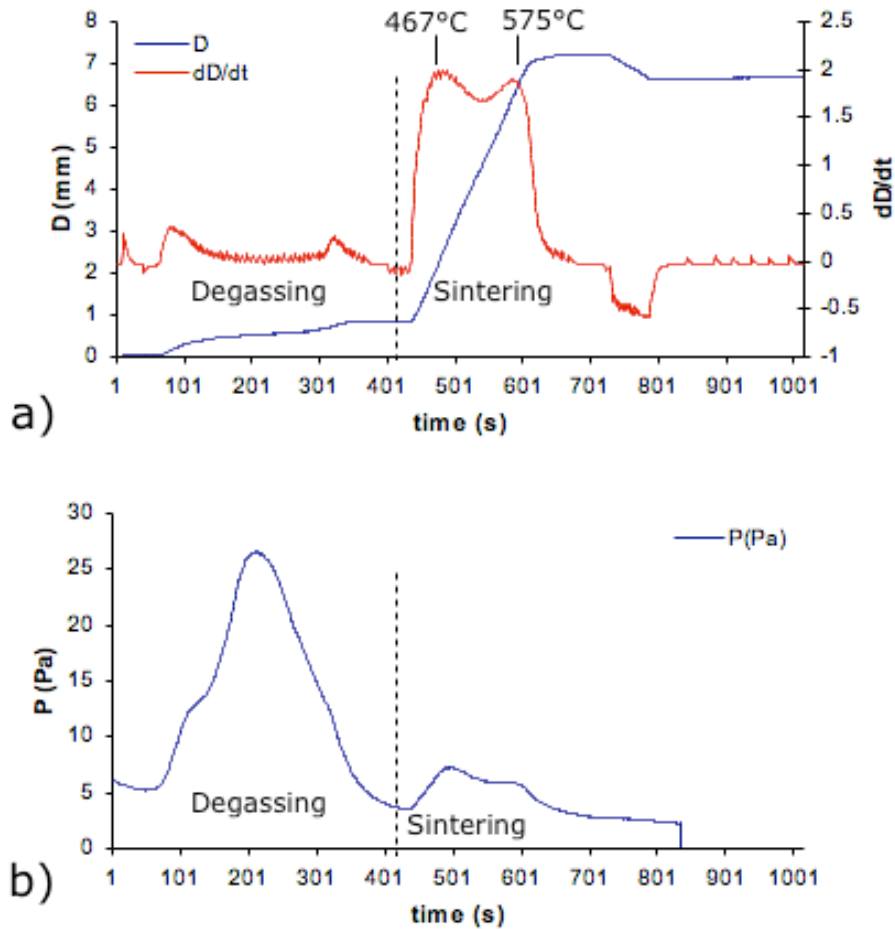


**Fig 18.** (a) Linear shrinkage curve and its derivative as a function of time for the nc-Al subjected to SPS at 60 MPa pressure and 620°C. The temperatures correspond to the maximum shrinkage rates during the sintering process. (b) The increases of pressure is proportional to the gas lost from the powder during the increases of temperature (degassing step).

The shrinkage was observed between 400°C and 600°C, because of the increasing pressure (from 5 to 60 MPa). Looking at the shrinkage derivative it is possible to recognize a double-peak. The first peak,

corresponding to a temperature of 467°C (around 0.70  $T_m$ ) might be related to the compaction of the powder and to the neck formation between particles due to the formation of the plasma (discharge due to the small contact area between particles). The second peak at 575°C (0.86  $T_m$ ) can be ascribed to the formation of large contact areas between particles accompanied by grain boundary and lattice diffusion. The plasma is proposed to cause a cleaning effect on the surface of the particles leading to a sintering enhancement. Many works have been devoted to the theory of the plasma [9-11] and has been doubted by others for lack of unambiguous experimental evidence [5, 12, 13]. It is reasonable to assume that the existence of plasma (discharge) must be evaluated taking into account both the role of applied pressure and the stage of sintering. This means that, if initially a discharge may be possible in conducting powders, as contacts between particles increase (due to the applied pressure and sintering), the probability of discharge phenomena becomes small. As a consequence, the sintering can be divided in two distinct steps as described above: first, the shrinkage at relatively low temperatures is due to the neck formation, assisted by the plasma; second, the contact between particles increases and sliding and diffusion related phenomena occur.

Finally, looking at Fig 18b, the first step of the SPS consolidation process was done without load applied to facilitate the degassing of the powder (mainly nitrogen during cryomilling). Fig 19 shows the differences between SPS consolidation process of cryomilled Al powder (granulometric fraction <25  $\mu\text{m}$  was used) previously degassed (18 h at 350°C and  $10^{-5}$  mbar) and the same powder in which the degassing process was done in situ during sintering. Both samples were consolidated at 620°C showing no relevant differences in terms of relative density (99.5% and 99.6% in the case of as-treated powder).

For this reason, the in situ degassing could constitute an opportunity to scale the entire process for the industrial application.

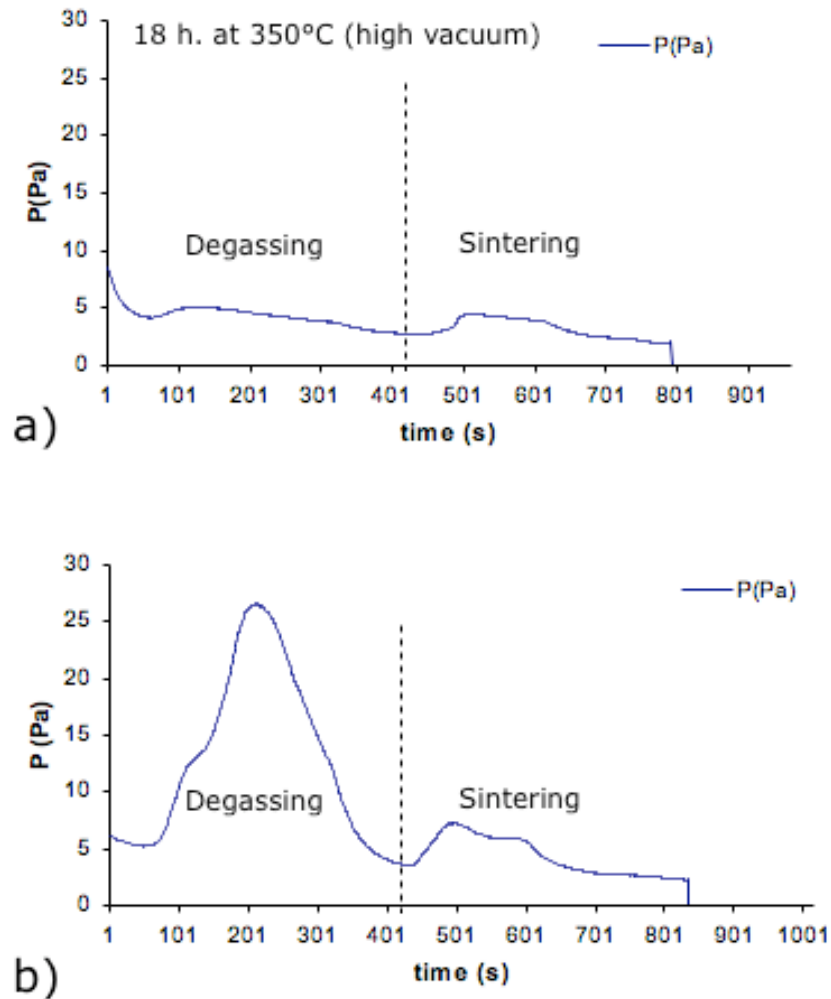


**Fig 19.** Pressure changes during the SPS consolidation process of the cryomilled Al powder (particle size  $<25 \mu\text{m}$ ). (a) Pre-degassed powder (18 h. at 350°C and  $10^{-5}$  mbar) and (b) as-milled powder.

### Microstructural characterization

Based on the results reported above, TEM examination of Al bulk samples obtained after sintering at 620°C (using powders with particle size <25 μm and 25-45 μm) was carried out. Fig 20 documents the microstructure (bright-field and the dark-field TEM images) of the bulk Al sample obtained using particles size <25 μm.

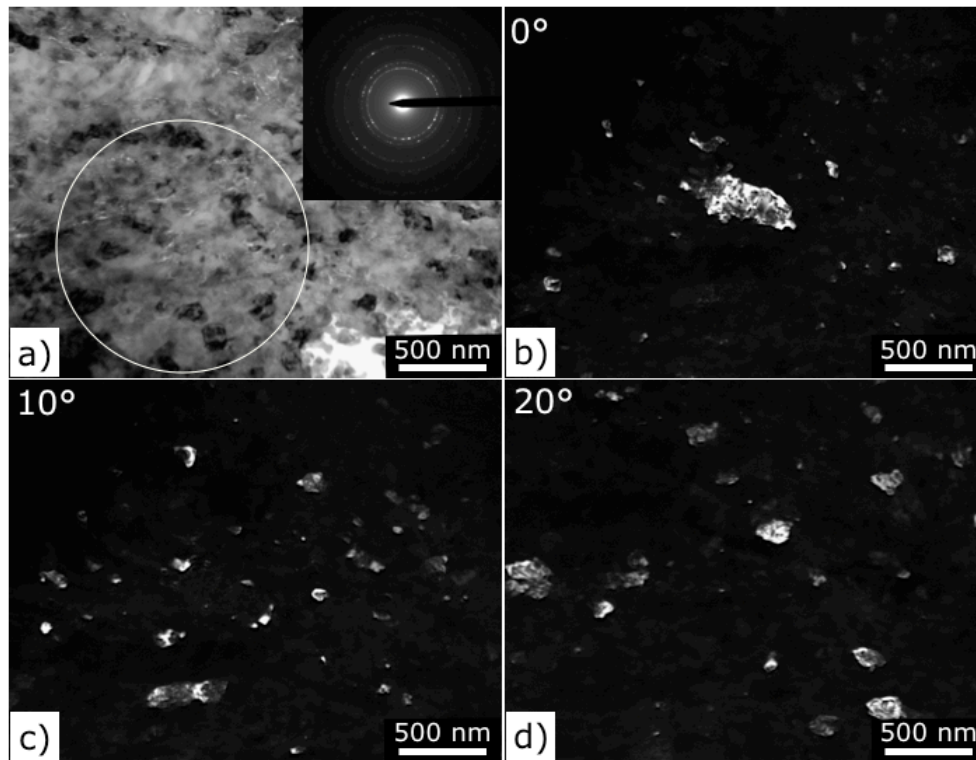


**Fig 20.** TEM image of the cryomilled Al specimen with a particle size <25 μm, consolidated at 620°C, under 60 MPa by SPS. (a) BF picture shows the microstructure and the selected area electron diffraction (SAED) pattern from the area identified by the circle. (b), (c) and (d) DF images collected by tilting the TEM sample from 0° to 20° show some ultrafine grains and nanocrystalline grains.

Fig 21 shows the TEM microstructures in the bulk Al obtained using the cryomilled particle size of the 25-45  $\mu\text{m}$  and a sintering condition of 620°C.

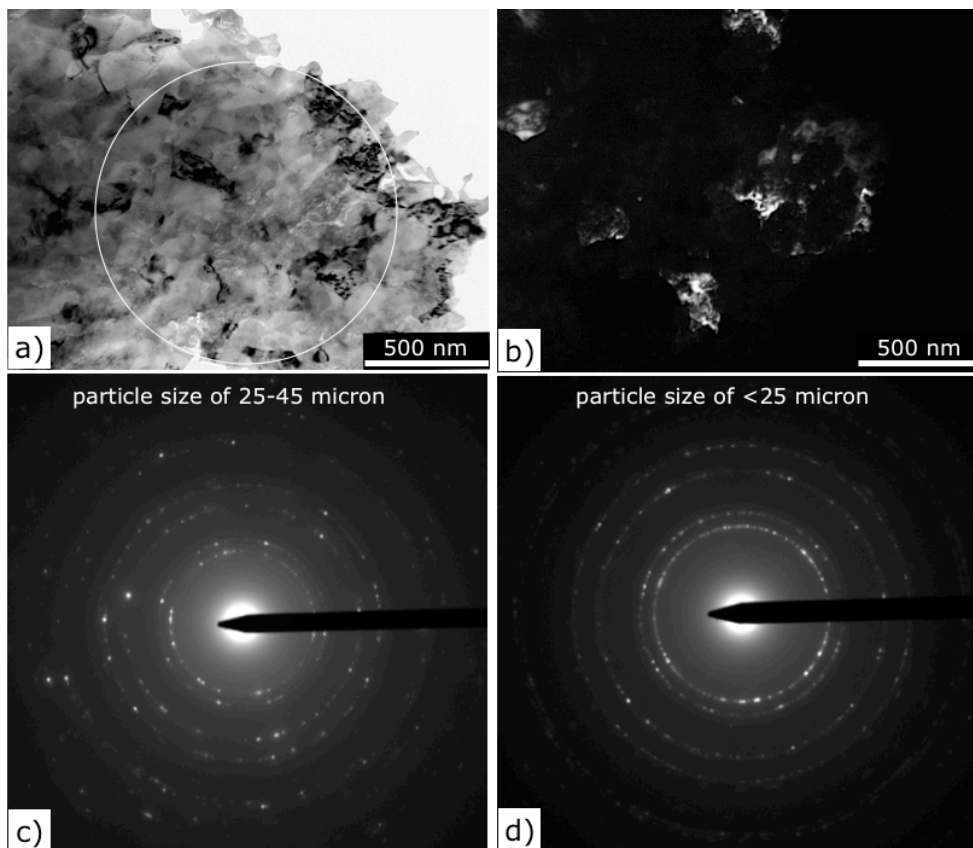


**Fig 21.** (a) BF and (b) DF TEM images of the bulk Al specimen consolidated at 620°C using cryomilled powder with a particle size of 25-45  $\mu\text{m}$ . SAED patterns collected with the same aperture show the differences between the as sintered 25-45  $\mu\text{m}$  (c) and the as sintered <25  $\mu\text{m}$  (d).

Both samples sintered at 620°C show a broad crystallite size distribution with ultra-fine grains of the order of 400 nm and grains smaller than 100 nm. However, the fraction of nanostructured grains is noticeably higher in the sample sintered at 620°C using the finer particle size (<25 μm). This fact can be experimentally observed looking at the BF and DF TEM images reported in Fig 20 and 21. Moreover, Fig 21c and 21d report the comparison between the electron diffraction patterns of the <25 μm sample and the 25-45 μm sample obtained with the same diffraction aperture. The number of grains that scatter producing diffraction rings in the <25 μm sample is much higher than for the 25-45 μm sample. The result is a homogeneous ring pattern (more small grains randomly oriented) with smaller spots (big grains).

Due to the aim of this thesis (study the deformation behavior in nanostructured bulk Al samples) from this point only the bulk sample obtained with the particle size <25 μm will be considered.

Looking again at the grain size in Fig 20, the DF images (Fig 20c and 20d) show that there is a sort of bimodal distribution in which the ultra-fine grains are embedded in a nanocrystalline matrix. This bimodal distribution of the grain size was confirmed performing line profile analysis on experimental data collected using high-energy X-ray diffraction from a synchrotron radiation source. The diffraction geometry and all the experimental procedures will be presented in the next chapter. Here we want to underline that the best fit was obtained using two different microstructural components to account for the bimodal grain size distribution and the possible anisotropic shape of the crystallites. The combined quantitative phase analysis and line-profile analysis show that the nanostructured volume fraction is around 60% with an average crystallite size of 87 nm. The remaining volume fraction of 40% is ascribed to the ultra-fine counterpart with an average

crystallite size of 280 nm. Fig 22 shows the XRD pattern (200 peak is enlarged in the inset).

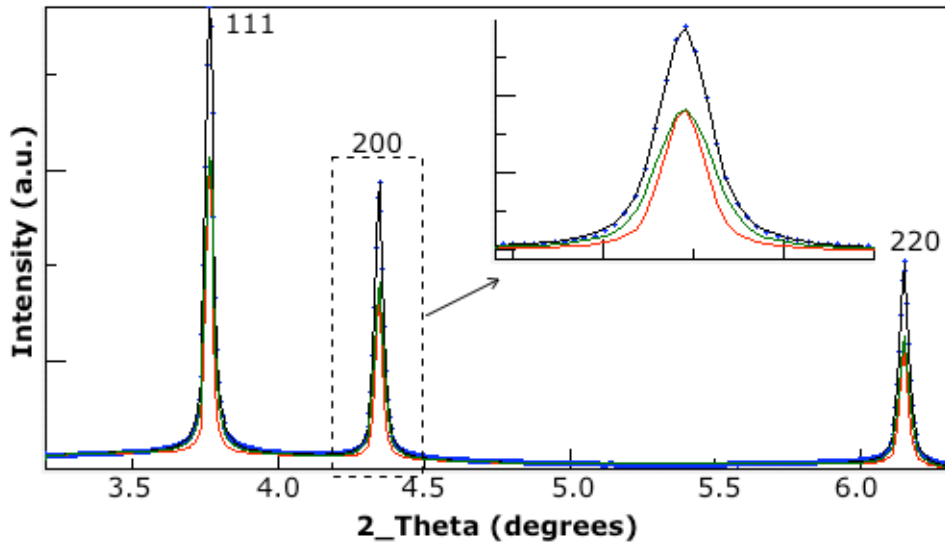


**Fig 22.** Experimental profile (blue dots) and recalculated (black line) for bulk nc-UF Al obtained after SPS consolidation and using the finer powder (particle size  $<25\ \mu\text{m}$ ). Green and red solid lines represent the deconvolution of the line profile into the nc and UF counterparts respectively.

The origin of this bimodal microstructure might be explained as follow. As reported by Yanagisawa [14], when copper powder particles were subjected to single-pulse discharges (500 ms duration) it was observed that sparks could form between some but not all particles.

It is reasonable to assume that, where the plasma forms, there is an abnormal grain growth due to the partial melting of the region, in which the pinning effect due to the presence of AlN or Al-oxynitride phases cannot oppose to the grain growth. In the rest of the sample, the grain

growth is strongly inhibited by the pinning effect ascribed to the second-phase particles. This explanation can be confirmed by investigating the microstructure in more detail. Fig 23a shows a BF image documenting an ultra-fine grain after abnormal grain growth in which the second-phase particles are clearly visible along the original grain boundaries. Fig 23b shows a nanostructured region in which nanopores at a grain boundary are highlighted by arrows. The electron diffraction analysis (Fig 23c and 23d) confirms undoubtedly the presence of hexagonal AlN and cubic  $\gamma$ -Al<sub>2</sub>O<sub>3</sub>.

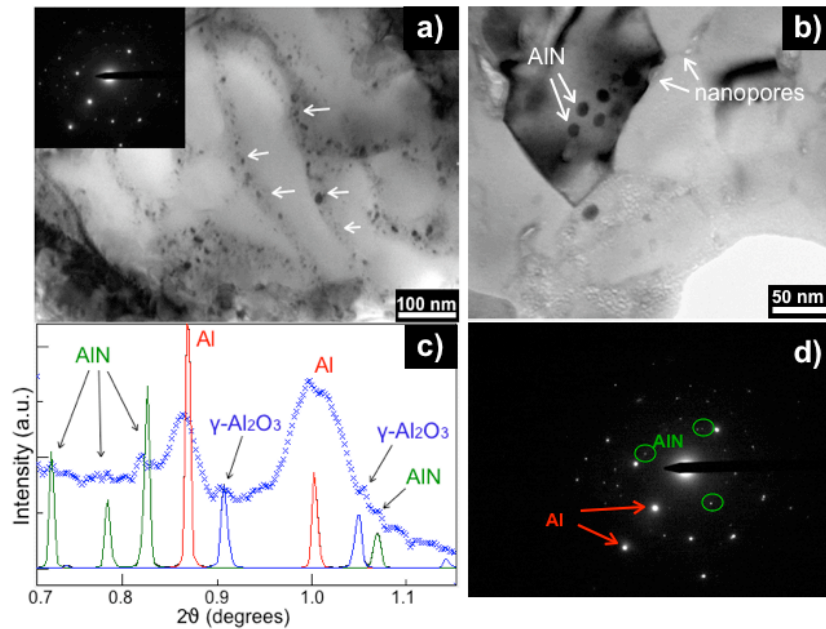


**Fig 23.** TEM bright-field images (a, b) and selected area electron diffraction (d) on the consolidated SPS powder. Only the finer granulometric fraction (<25  $\mu$ m) was used. Phase identification reported in c shows the presence of hexagonal AlN and cubic Al<sub>2</sub>O<sub>3</sub>. Nanopores are clearly visible in Fig 20b.

This confirms that while  $\text{Al}_2\text{O}_3$  particles might be due to the presence of the oxide layer that covers the Al powder particles before milling, the formation of AlN is the result of milling in the liquid nitrogen environment. The microstructural characterization of the SPS consolidated samples confirms that the exceptional thermal stability of nanostructured Al obtained by cryomilling reported in the previous chapter is due to the drag stress exerted by grain boundary impurities, second phase particles and nanopores.

In the next chapter the mechanical response of this microstructure will be analyzed in detail.

### **Summary**

Bulk nanocrystalline/ultrafine Al samples were produced using spark plasma sintering consolidation method. The first step of the SPS consolidation process was done without load applied, to facilitate the degassing of the powder. However, in order to activate grain growth and reach a sufficient degree of compaction (99.5% relative density) the sintering temperature had to be increased up to 620°C. During SPS we can identify two distinct phenomena:

(a) a first shrinkage at relatively low temperatures (470°C) in which the neck formation between particles, assisted by the plasma takes place, (b) a second shrinkage at high temperature (575°C) where the contact between particles increase and sliding and diffusion related phenomena occur.

Both TEM analysis and high-energy synchrotron X-ray diffraction confirm a broad crystal size distribution with a bimodal microstructure in which ultrafine grains are embedded in a nanocrystalline matrix. The presence of AlN and Al oxides detected by selected area electron diffraction

analysis explains the exceptional thermal stability described in chapter 1. It is reasonable to assume that, the ultrafine grains are originated where the plasma forms. In these regions a partial melting can occur with a subsequent enhancement of grain growth.

## References

- [1] M. Tokita, Sumitomo Coal Mining Company, Internal Communication 11pp.
- [2] M Tokita: Proc. NEDO Int. Symp. On "Functionally graded materials, Tokyo, Japan, October 1999, New Energy and Industrial Technology Development Organization, 23-33.
- [3] M. Omori: Mater Sci Eng A, A287 (2000) 183.
- [4] M. Nygren, Solid State Sci, 5, (2003), 125.
- [5] G. Xie, O Ohashi, K Chiba, N Yamaguchi, M Song, K Furuya and T. Noda, Mater Sci Eng A, A359 (2003) 384.
- [6] M Zadra, F Casari, L Girardini, A Molinari, Powder Metallurgy, 50 (2007) 40.
- [7] U Anselmi-Tamburini, J E Garay, Z A Munir, A Tacca, Z Maglia, G. Spinolo, J. Mater. Res. 19 (2004) 3255.
- [8] Z A Munir, U Anselmi-Tamburini, M Ohyanagi, J. Mater. Sci. 41 (2006) 763.
- [9] M Tokita, Mater. Sci. Forum 308-311 (1999) 83.
- [10] Z. Shen, M. Johnsson, Z. Zhao, M. Nygren, J. Amer. Ceram. Soc. 85 (2002) 1921.
- [11] M. Omori, Mater. Sci. Eng. A287 (2000) 183.
- [12] M. Nygren, Z. Shen, Solid State Sci 5 (2003) 125.
- [13] S. W. Wang, L. D. Chen, T. Hirai, Y. S. Kang, J. Mater Sci Lett. 18 (1999) 1119.

- [14] O. Yanagisawa, H. Kuramoto, K. Matsugi, M. Komatsu, Mater Sci Eng A350 (2003) 184.

### **3. Deformation mechanism and plastic strain recovery in bulk bimodal nc-UF aluminum**

#### **Introduction**

In general, the strength and the ductility of materials are directly correlated to the microstructure and, for polycrystalline metals the grain size and the linear crystalline defects (dislocations) are two of the most important variables. An increase of strength can be reached by introducing microstructural obstacles to dislocation motion. These obstacles are: solid solution atoms, second-phase particles and the increase of the grain boundary volume fraction with decreasing grain size. The general realization that a material with high density of grain boundaries is stronger than a coarse-grained material with low density of grain boundaries, is well summarized by the Hall-Petch relationship (H-P) [1, 2]:

$$\sigma_y = \sigma_0 + K_y d^{-1/2}$$

where  $d$  is the mean grain size and  $\sigma_0$  and  $K_y$  are constants. This relation is always obeyed for ductile metals with grain size in the range of micrometers. Below micrometric grain size in the range of ultra-fine grains (150-500 nm) or nanometric grains (30-150 nm) still the available data follow H-P. Below this limit, there are uncertainties regarding the effective softening trend that is reported, see e.g. [3-5]. As the grain size decreases, the quantity of grain boundaries increases, increasing also the fractions of atoms that lie in this region. We note that the situation is very different: for an average grain size of 3  $\mu\text{m}$ , the fraction of atoms that constitute the grain boundary is about 0.01%

but for a grain size around 30 nm the proportion of atoms involved reaches 1% [6]. Moreover, the traditional description of grain boundaries with static geometric structures depicted as, e.g., coincidence site lattice fails when the grain size reaches the nanometer scale. At this level many of the dislocation mechanisms that govern the plastic deformation are no longer geometrically reasonable and recent studies suggest that grain boundaries are not static entities [7-12]. These observations report a tendency for nanocrystalline metals of very high purity (99.999%) to grow spontaneously in a matter of days at room temperature with a significant acceleration upon the application of stress. In metals of commercial purity the driving force for grain growth, associated with the large energy due to the high density of grain boundaries, is inhibited by impurities that tend to stabilize the nanostructure [11]. Consequently we have to take into account that the deformation behavior in nanostructured bulk aluminum obtained after cryomilling and SPS consolidation will be affected also by the impurities that are present during the entire fabrication process.

It is widely acknowledged that shear stresses drive the dislocation motion. These dislocations usually arranged in low angle grain boundaries can be moved under applied stress. The low angle grain boundaries motion can be explained as a collective movement of the individual dislocation in these boundaries [13, 14].

A very recent study [15] shows that for freestanding nanocrystalline aluminum thin films (very high purity) the driving force to move the high-angle grain boundaries is also attributable to shear stresses. This study proves that the grain boundaries are not stationary obstacles to dislocation-based plasticity but the shear stresses drive grain boundaries to move, in accordance with the recent molecular dynamic simulations [16, 17]. However, as previously reported, the mobility of high-angle grain boundaries can be limited or even inhibited by the presence of

solute atoms or second-phase particles always present in commercial nanostructured bulk metals. In this scenario a couple of questions become important: first, is it possible to approach the study of the deformation behavior of nanostructured aluminum using the unified theory of coupled grain boundary motion taking into account the drag effect induced by impurities?

Second, the interaction between two opposite phenomena, the drag effect induced by impurities and the grain boundary migration induced by shear stress could be experimentally detected as phenomena like grain rotation?

Here below we report the four fundamental phenomena associated with grain boundaries and recently reported in the unified approach proposed by Cahn and co-workers [16, 18]:

1. Normal motion (migration) where the GB moves along its normal direction. The GB velocity  $\mathbf{v}_n$  is parallel to the GB normal vector  $\mathbf{n}$  (normal to the shear stress vector  $\boldsymbol{\tau}$ ). The dynamics of the GB is characterized by the growth of one grain into another. The GB is at the same time a front of grow and dissolution.
2. Relative translation of the grains parallel to the GB plane coupled by normal motion of GB along its normal direction. We can identify two different GB velocities, one parallel to the GB normal vector  $\mathbf{n}$  ( $\mathbf{v}_n$ ) and another parallel to the shear stress vector  $\boldsymbol{\tau}$  ( $\mathbf{v}_{||}$ ).
3. Relative rigid-body translation of the grains along the GB (parallel to the shear stress vector  $\boldsymbol{\tau}$ ) by sliding ( $\mathbf{v}_{||}$ ).
4. Grain rotation, where there is a change of misorientation across the GB. This process is always coupled by the relative translation.

Particularly, we should imagine that all GB's are actually curved. This implies that curvature-driven coupled GB motion should almost always be accompanied by grain rotation. In parallel, a shear stress applied

along a curved GB not only leads to a grain rotation but also creates an additional driving force for a GB motion. The grain growth and the grain rotation of nanocrystalline metals, particularly during plastic strain, is well experimentally documented in the recent literature [9, 19].

But we must take into account the following consideration: in nanocrystalline metals the conventional sources of dislocations that are common in coarse grain metals (intragranular dislocation sources such as Frank-Read source) cease to operate and the deformation mechanism could be diffusive (sliding) and/or displacive thanks to the generation and subsequent annihilation of partial dislocation at the GB's. Recently, a quantitative description of plastic deformation in nanocrystalline copper shown that the contribution of diffusive mechanisms such as GB sliding are actually a minor part of the deformation mechanism even at very small grain size (5-10 nm) [20]. Moreover, molecular dynamic simulations suggest that plastic deformation in nanocrystalline metals is carried out by dislocation nucleated at the grain boundaries [21-23]. Related also to the dynamics of dislocations during plastic strain in nanocrystalline metals and to the particular role covered by a dynamic interpretation of the GB, Rajagopalan and his research group have documented that freestanding aluminum and gold nanocrystalline thin films with an average grain size around 60 nm, recover a substantial fraction of plastic deformation after unloading and under macroscopically stress-free conditions [24]. This important reference report the following observations:

1. Nanocrystalline aluminum and gold thin film specimens recover a substantial fraction of plastic deformation after unloading.
2. After strain recovery, the specimens show no residual hardening during the next loading
3. The strain recovery occurs under a macroscopically stress-free condition showing a time-temperature dependence.

This work reported here above, follows another important experimental contribution that describes, using in-situ synchrotron X-Ray technique, the complete recovery of the peaks broadening after plastic deformation of electrodeposited nanocrystalline nickel [25]. This means that the deformation process does not build up a residual dislocation network.

All these experimental and theoretical studies confirm that, even in nanostructured metals, the main deformation mechanism remains correlated to the generation and annihilation of partial dislocations at the GB's. The behavior of the GB remains absolutely dynamic and, diffusive mechanisms such GB sliding are of minor importance. The state-of-the-art illustrated here can be summarized in the following three points:

First, from experimental results and theoretical interpretation we have to consider the GB as a dynamic entity where GB motion, GB rotation and generation/recombination of dislocations are always possible.

Second, the interaction with impurities such solute atoms or second-phase particles affects the mobility of the GB and the grain growth observed for very high purity samples is partially or completely inhibited.

Third, plastic strain recovery and recovery of dislocations in nanostructured Al, Au and Ni thin films were experimentally observed.

On the basis of these exciting results that describe the strain behavior in nanostructured thin films we performed a study of deformation mechanisms involved in bulk nanostructured aluminum samples obtained after cryomilling and subsequent SPS consolidation process. The stimulus for this work was the paper published two years ago in Science by Rajagopalan and co-workers in which a surprising plastic strain recovery was observed in the nanocrystalline electrodeposited thin films of fcc metals. The first part of this chapter will be dedicated to present the experimental techniques and the theory. In

the second part we will describe the results obtained after ex-situ and in-situ deformation experiments.

The work is the result of a collaborative project between University of Trento, Argonne National Laboratory (APS, Chicago) and Los Alamos Neutron Science Center (LANCE, NM). These in situ high-energy synchrotron and neutron diffraction experiments, particularly during unloading were necessary in order to explain why the plastic strain can recover. We will present experimental evidences that are simply fascinating describing the interaction between nanocrystalline regions and ultrafine grains during the entire loading-unloading cycles and the surprising evolution of the lattice preferred orientation that is able to recover after unloading.

## **Experimental procedure**

### *Compression experiments*

As previously discussed, bulk nanocrystalline/ultrafine (nc-UF) samples (cylinders of 20 mm diameter and 10 mm high) were obtained by SPS consolidation. The first idea was to test the samples in compression. In contrast to tension, large plastic strains can be obtained during compression without any instability that could affect the response of the material. Particularly, the goal of this first set of experiments was to verify if the bulk nanostructured Al could recover a significant part of plastic deformation after unloading, as reported for nanostructured thin films [24]. Moreover, to verify if the plastic strain recovery is also thermally activated, the samples had to be heated and cooled to analyze the expansion, the contraction and the final length of the samples after the thermal cycles. To perform compression and annealing experiments

a Baehr Dilatometer 805 A/D (Fig 24) equipped with a compression head was used. This special dilatometer is dedicated for the determination of deformation parameters and for the creation of continuous cooling and isotherm TTT-diagrams. In order to insure uniformity among the samples used in the compression tests, the original cylinder (from SPS, 30mm diameter and 10mm high) was cut into several cylindrical samples with 4.5 mm diameter and 10 mm high by electrodischarge machining (EDM). The cylinders were polished to produce parallel flat faces with a final polish consisting of a 1  $\mu\text{m}$  diamond suspension. All the tested samples were compressed using the same deformation rate of 0.01 mm s<sup>-1</sup> (strain rate of 10<sup>-3</sup> s<sup>-1</sup>). The instrument resolution of displacement ( $\Delta l$ ) is 0.05  $\mu\text{m}$  and of temperature is 0.05°C.



**Fig 24.** Baehr plasto-dilatometer 805 A/D equipped with a compression head

We have tested two different series of samples having different microstructure. The first sample called C (coarse) is a reference Al sample obtained using the as-atomized powder (no cryomilled) and

sintered at 600°C and 60 MPa (full density, >99%). The microstructure is characterized by coarse grains ranging between 20 and 90  $\mu\text{m}$ .

The second sample called nc/UF was well characterized in the previous chapter and shows a bimodal microstructure, with an average crystallite size of 87 nm (60%) and a minor part of grains that are in the range of 200-400 nm (40%). Table 1 reported below summarizes all the compression experiments schedule performed using the Baehr dilatometer 805A/D.

**Table 1.** Deformation recovery experiments on Al samples

Sample	Microstructure	Strain rate	Strain (recovery at 0 MPa)
C	Coarse (>20 $\mu\text{m}$ )	$10^{-3}$	RT up to 3.6% and 4.2%
C	Coarse (>20 $\mu\text{m}$ )	$10^{-3}$	RT up to 3.6% and 4.2% +180°C
A-nc/UF nano	(<85 nm)	$10^{-3}$	RT up to 2.6%
B-nc/UF nano	(<85 nm)	$10^{-3}$	RT up to 3.6%
D-nc/UF nano	(<85 nm)	$10^{-3}$	RT up to 4.3% (5 cycles)
E-nc/UF nano	(<85 nm)	$10^{-3}$	RT up to 1.8%+2%+3%+4%+180°C

#### *In-situ synchrotron X-ray and neutron diffraction experiments*

In this study, *in-situ* synchrotron X-ray and neutron diffraction were employed to study the deformation behavior of single-phase fcc nc-UF

bimodal bulk Al and a coarse-grained Al reference sample. Neutron and high-energy X-ray from synchrotron source have both strong penetration capabilities. These two techniques are able to investigate structural changes at the grain size level in bulk specimens. Recently, they have been employed to characterize the deformation behavior of nanostructured and large-grained composites [26, 27], nanostructured biological samples [28] and nanostructured and large-grained metals [29, 30].

For Synchrotron XRD experiments a parallelepiped ( $2.5 \times 2.5 \times 5 \text{ mm}^3$ ) of bulk nc-UF Al was studied. The sample was deformed in situ using a screw-driven load frame while being interrogated with high-energy X-rays (monochromatic wavelength of  $0.15359 \text{ \AA}$  and a beam size of  $60 \times 60 \text{ }\mu\text{m}$ ) at sector 1-ID at the Advanced Photon Source (Argonne, USA). Transmission diffraction pattern were recorded from the central region of the sample using a MAR 345, image plate detector ( $3450 \times 3450$  pixels), mounted perpendicular to the incident beam behind the sample. By using area detector and high-energy X-rays (and associated small  $\theta$ ), scattering from the load and transverse directions was collected simultaneously, over a q-range covering the Al 111, 200 and 220 reflections. The sample was loaded in 100 MPa steps to 400 MPa, and then unloaded, with diffraction data collected for 30 s at every 100 MPa interval. Fig 25 shows the geometry of the experimental setup.

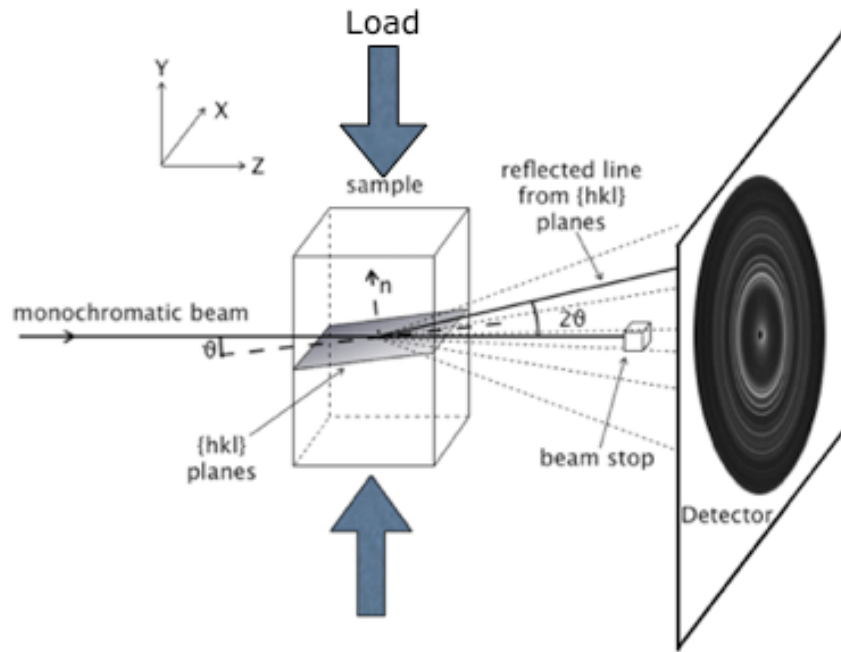


**Fig 25.** Diffraction geometry of the in-situ synchrotron experiments in transmission. The samples are loaded and unloaded along the Y axis. The X-rays interacting with specific hkl planes are diffracted at a defined  $2\theta$  angles are collected using 2D area detector (MAR345).

Diffraction data were converted to TIFF images, using the FIT2D software package [31], and then integrated over five degrees azimuthal sectors to produce 72 one-dimensional lineouts (Fig 26a and b). A reference of ceria (NIST SRM-674a) and silicon (NIST SRM-640c) were used to calibrate the instrumental parameters and the peak-broadening function for the integrations.

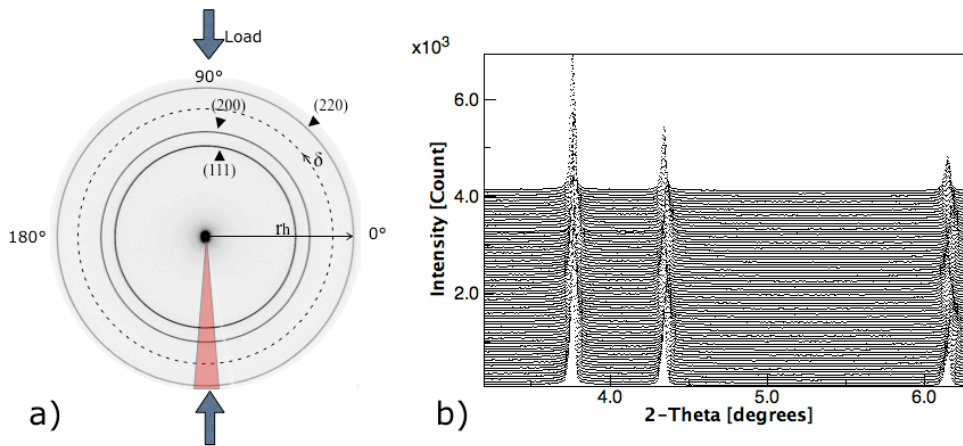


**Fig 26.** (a) Two dimensional synchrotron diffraction image of nc-UF aluminum used in the Rietveld analysis. One five degrees azimuthal sector along the loading direction enhanced with red color. (b) 72 experimental diffraction spectra generated by the integration of the 2D diffracted image. Note the peak shifting due to the deviatoric stress.

For neutron experiments a cylinder of 10 mm diameter and 25 mm length of bulk coarse Al was used to follow the texture and the strain evolution during plastic deformation. Neutrons can penetrate further in to the sample (several mm) providing information representative of the bulk behavior with a good statistic even if the average grain size is big. For this reason the present study was conducted on the Spectrometer for Materials Research at Temperature and Stress (SMARTS) [32] diffractometer at Los Alamos National Laboratory (NM, USA), utilizing a polychromatic beam from a spallation neutron source with detectors in two fixed orientations (Fig 27a). SMARTS has two banks of detectors—Bank1 oriented for measurements from lattice planes whose normals are perpendicular to the loading axis and Bank2 oriented for measurements from lattice planes whose normals are parallel to the loading axis (Fig 27b).

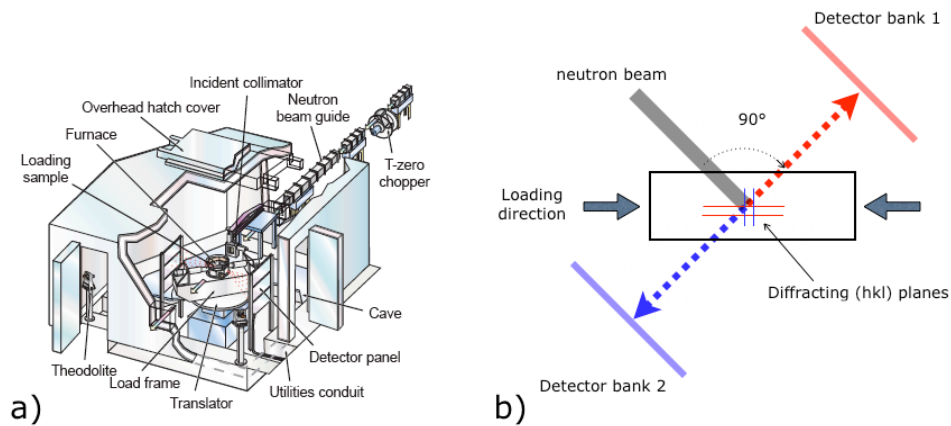


**Fig 27.** (a) SMARTS diffractometer at Los Alamos national laboratory. (b) Diffraction geometry shows the scattering vectors of planes parallel and normal to the loading axis collected from detector bank 2 and detector bank 1 respectively.

These two detectors are constituted with a total of 384 single ended  $^3\text{He}$  tubes, mounted on either side of the incident beam with a secondary flight path of 1.5 m to the sample at  $\pm 90^\circ$ . The detectors are connected to TOF (time of flight) modules. With the TOF technique, the data acquisition time is reduced since spectra with many hkl diffraction peaks are measured simultaneously [33]. The collected spectra during loading and unloading from the two detectors are characterized by the shift in the peak position that represents the elastic lattice strains and can be measured from either single peak fitting or lattice parameter refinement from the Rietveld method (see the next section). The variation in the peak intensity represents the development of Lattice Preferred Orientation (LPO) as a result of the plastic deformation (see

the next section). Fig 28 shows the experimental spectra of coarse aluminum collected from detector bank 1 and 2 at 9.5% of strain.

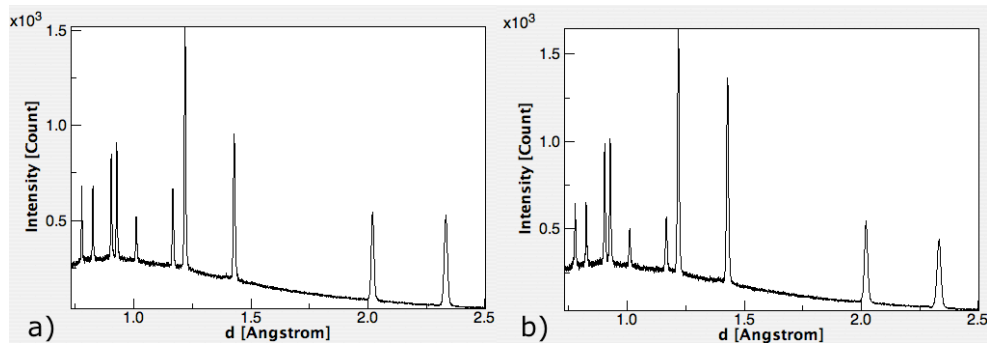


**Fig 28.** Example of Lattice preferred orientation developed in coarse Al sample during compression. A significant change in the reflection relative intensities is observable for the two sample orientation representatives of hkl planes that are normal (a) and parallel (b) to the loading direction.

## Data analysis

### Rietveld method

The synchrotron and neutron diffraction spectra were analyzed with the Rietveld method [28, 34] as implemented in the program package MAUD (Materials Analysis Using Diffraction) [35, 36].

Rietveld refinement was originally introduced for the analysis of constant wavelength neutron diffraction data [37, 38] and was subsequently used to refine data from conventional X-ray and Synchrotron diffraction experiments. In Rietveld analysis, a least squares method is used to obtain the best possible fit between the

complete experimental diffraction pattern and a corresponding calculated one. The calculated pattern is directly correlated to the crystal structure of the material analyzed. The intensity depends on numerous factors and can be determined from the following equation [39]:

$$Y_{ci} = s \sum L_K |F_K|^2 \phi(2\theta_I - 2\theta_K) P_K A + Y_{bi}$$

Where,  $s$  is the scaling factor,  $K$  the triplet of  $h$ ,  $k$  and  $l$  Miller indices for a Bragg reflection,  $L_K$  is representative for the Lorentz, polarization and multiplicity factors,  $F_K$  the structure factor,  $\phi$  the reflection profile function,  $2\theta_I$  the observed peak position,  $2\theta_K$  the calculated position of the Bragg peak corrected for the zero-point error in the detector,  $P_K$  the preferred orientation function (presence of crystallographic texture),  $A$  an absorption factor and  $Y_{bi}$  is the background intensity at the  $i$ th step of the iteration process. In order to obtain a good fit between the experimental and the recalculated spectra a number of parameters such as atom position, thermal factors (isotropic or anisotropic), site occupancy, lattice, background, instrumental and profile parameters are typically refined. Particularly, the profile function may include effects from crystallite size and microstrain (peak broadening), specimen and instrumental source and geometry. Moreover, the presence of preferred orientation necessitates the refinement of texture.

#### Lattice Strain determination

As previously reported, MAUD software was used to extract structural and microstructural information from the synchrotron and neutron diffraction data. The software has multiple applications for a wide range of materials and diffraction techniques. Instrument-specific parameters

are required (e.g. for conventional X-rays, synchrotron X-rays, low-angle scattering, neutrons); phases need to be characterized (crystallography/structure, microstructure, texture, elastic strain); various diffraction data sets can be entered (in this study TOF neutron diffraction data in GSAS format, and synchrotron data in ESRF and APS formats).

For synchrotron data triaxial stress model (included in MAUD) with Young's modulus ( $E$ ) and Poisson's modulus ( $\nu$ ) fixed as constants (71 GPa and 0.33, respectively) was applied to account the first-order macroscopic strain (averaged over all grains within the macroscopic irradiated volume) induced by macroscopic external stress applied. To calculate internal stresses along the loading direction, strains  $\epsilon_{xx}$  and  $\epsilon_{yy}$  where measured. Here  $x$  and  $y$  directions are along to the horizontal and vertical axes of the 2D diffraction pattern and X-ray beam is along  $z$  (Fig 25). The internal stress along the loading direction can be described by the following equation:

$$\sigma_{yy} = \frac{1}{S_2/2} \left[ \epsilon_{yy} - \frac{S_1}{S_2/2 - 3S_1} (\epsilon_{yy} + 2\epsilon_{xx}) \right]$$

where  $S_1 = (-\nu/E)_{average}$  and  $S_2/2 = ((1 + \nu)/E)_{average}$

For neutron diffraction data, the histogram from the Bank 2 detector (representing measurements from lattice planes whose normals are parallel to the axis of loading) was considered to refine the lattice parameter. The lattice parameter obtained from Rietveld refinement was used to obtain the lattice spacings  $d^{hkl}$  from:

$$\frac{1}{(d^{hkl})^2} = \frac{4}{3} \left[ \frac{h^2 + hk + k^2}{a^2} \right] + \frac{l^2}{c^2}$$

The strain for a specific hkl plane can be obtained using the following equation:

$$\varepsilon_{hkl} = \frac{d^{hkl} - d_0^{hkl}}{d_0^{hkl}} .$$

#### Microstructural determination

For line profile analysis, standard samples to calibrate the instrumental function were used for both synchrotron (Si-NIST640c) and neutron (Al coarse stress free and isotropic sample) experiments. It should be noted that, to account a possible anisotropy of the crystallite size and microstrain for the different hkl direction during plastic deformation, the diffracted peaks must be treated independently each other.

Using the Popa approach [40], the anisotropic crystallite size (D) and microstrain ( $\langle \varepsilon^2 \rangle^{1/2}$ ) were evaluated. According to the Popa model,  $\langle R_{hkl} \rangle$  can be considered the mean crystallite size in the crystal direction  $\langle hkl \rangle$  so  $\langle R_{hkl} \rangle$  can always be developed in a convergent series of symmetrized spherical harmonics. For the Laue group m3m,  $\langle R_{hkl} \rangle$  is expressed as

$$\langle R_{hkl} \rangle = R_0 + R_1 K_4^1(x, \phi) + R_2 K_6^1(x, \phi)$$

with:

$$K_4^1(x, \phi) = 0.3046972 P_4^0(x) + 0.3641828 P_4^4(x) \cos 4\phi$$

$$K_6^1(x, \phi) = -0.1410474 P_6^0(x) + 0.527751 P_6^4(x) \cos 4\phi$$

The first term  $R_0$  correspond to the mean crystallite size over all the **hkl** directions,  $x = \cos \chi$ ,  $P_l^j$  is the Legendre function and  $\chi$  and  $\phi$  are the polar and azimuthal angles in a crystallite orthogonal coordinate system.

The microstrain series developed for the cubic system is:

$$\langle \varepsilon_{hkl}^2 \rangle E_{hkl}^4 = E_1(h^4 + k^4 + l^4) + 2E_2(h^2k^2 + h^2l^2 + k^2l^2).$$

#### Quantitative texture analysis

The quantitative determination of the texture is based on the concept of Orientation Distribution Function (ODF)  $f(g)$ . This function represents the statistical distribution of the orientations of the constitutive crystallites in a polycrystalline aggregate. The ODF maps the probability of each of the possible grain orientation with respect to the external sample dimensions and the integration is over all orientation space. Considering a sample with an irradiated volume  $V$  (diffraction experiment) it is possible to write the following equation:

$$\frac{dV(g)}{V} = \frac{1}{8\pi^2} f(g) dg$$

where  $dg = \sin\beta d\beta d\alpha d\gamma$  in the orientation element defined by three angles  $g = \{\alpha, \beta, \gamma\}$  (Fig 29) in the orientation space, that bring a given crystal coordinate system  $K_B$  co-linear with the sample coordinate

system  $K_A = (X, Y, Z)$  or  $(100, 010, 001)$ .

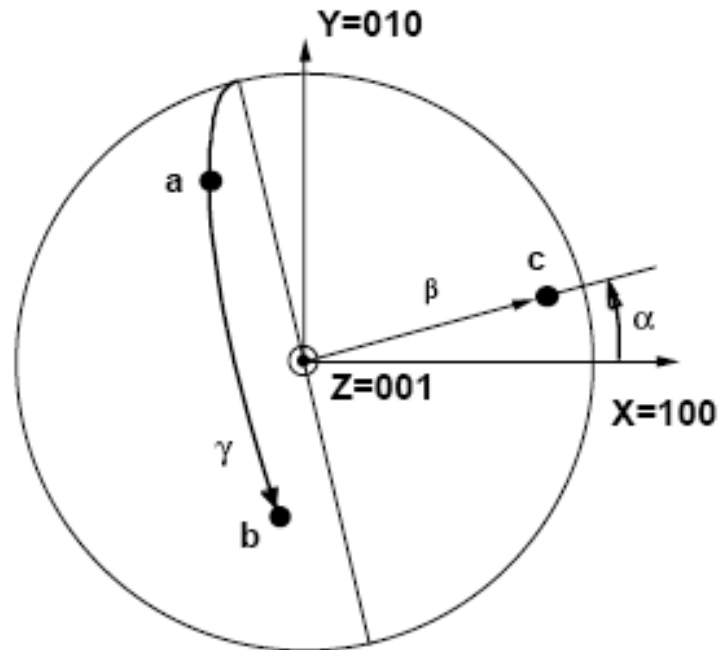


**Fig 29.** Definition of the three Euler angles that define the position of the crystallite co-ordinate system  $K_B=(a,b,c)$  of an orthogonal crystal cell in the sample coordinate system  $K_A=(X,Y,Z)$ . The 100, 010 and 001 are not Miller indices but vectors referring to an orthonormal frame aligned with  $K_A$ .

The two first angles  $\beta$  and  $\alpha$  determine the orientation of the  $[001]$  crystallite direction in  $K_A$  called pole distance and azimuth respectively. The angle  $\gamma$ , defines the location of another crystallographic direction, chosen as  $[010]$ . Finally,  $dV(g)$  represents the volume of crystallites which orientation is between  $g$  and  $g+dg$ .

The function  $f(g)$  then represents the volumetric densities of crystallites oriented in  $dg$ . It is measured in mrd (multiples of a random distribution) and normalized to the value  $f_r(g) = 1$  mrd for a sample

without any preferred orientation (random or powder). These values are called orientation distribution densities, and the function  $f(g)$  can take values from 0 (absence of crystallites oriented in  $dg$  around  $g$ ) to infinity (single crystals with planes oriented in  $dg$  around  $g$ ).

Here we report a short paragraph describing in which way the changes in peaks intensity due to preferred orientation can be measured and quantified.

Experimental measurements are the so-called direct pole figures,  $I_h(\mathbf{y})$ , with  $\mathbf{h} = \langle hkl \rangle$  (an  $hkl$  crystal plane orthogonal to the  $h$  direction) and  $\mathbf{y} = \{\alpha, \beta\}$ . The diffracted intensities  $I_h(\mathbf{y})$  depend on the porosity, crystalline state and others features of the sample. To compare samples between each other a quantity only depending on the orientation has to be calculated. This quantity is the normalized pole figure  $P_h(\mathbf{y})$  representing the distribution densities of  $\mathbf{h}$  directions on the pole sphere (Fig 30).

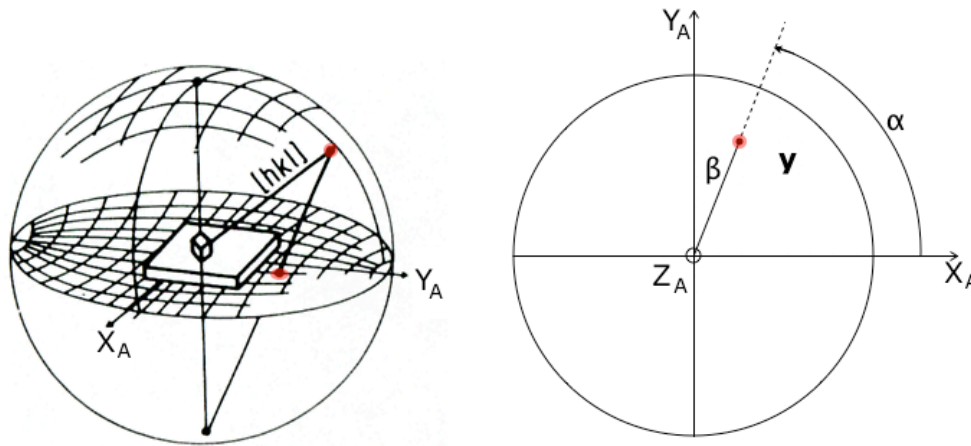


**Fig 30.**  $\{hkl\}$  pole figure co-ordinates in the sample reference frame  $K_A$ .

This angular distribution is defined by the volumetric function  $dV/V$  of the crystallites with the direction  $\mathbf{h}$  (of a generic plane  $hkl$ ) parallel to the sample direction  $\mathbf{y}$ . This concept can be described by the following equation:

$$\frac{dV}{V} = \left( \frac{1}{4\pi} \right) P_h(y) dy$$

where  $y = \{\alpha, \beta\}$  and  $dy = \sin\alpha \, d\alpha \, d\beta$ .

Commonly, a polycrystalline sample is constituted by several crystallites, each of them with different crystallographic planes with normal vectors associated. Consequently each plane can be identified by a certain direction ( $h$ ) that can be correlated to the reference direction  $y$  (sample direction). However, one pole figure is only a measure of the distribution of one direction type  $\langle hkl \rangle$ . Any rotation around this direction by a  $\chi$  angle results in the same diffracted intensity. Thus, the polar density in  $\mathbf{y}$  comes from every crystal with a direction  $\mathbf{h}$  parallel to the direction  $\mathbf{y}$ . The fundamental equation of texture analysis can be writes as follows:

$$P_h(y) = \frac{1}{2\pi} \int_{h//y} f(g) d\chi$$

where  $\chi$  represents the rotation of the crystal around the common direction  $h//y$ .

This equation represents the fact that each pole figure (a 2D object) is a projection along a certain path  $\chi$  of the ODF (a 3D object), which of course depends on the crystal symmetry. Each cell of a given pole figure will then be an average over several cells of the ODF, and each cell of

the ODF will be measured by one more cells from the pole figures. The larger the number of pole figure cells that measure a specific ODF cell and the more statistically reliable is the measurement of this ODF. In practice, one has to measure the largest number as possible of reliable (enough intense) pole figures to define the ODF with the best resolution available.

For cubic materials like aluminum the definition of three pole figures for three different hkl planes are sufficient to define a reliable ODF [41]. In this work for in-situ synchrotron diffraction experiment on nc-UF aluminum, the pole densities were then used to calculate the grain orientation distribution function of the sample for each stress (during loading and unloading) using the tomographic EWIMV algorithm that is related to WIMV (Williams-Imhof-Matthies-Vinel) [42], capable of processing incomplete pole density distribution on irregular coordinate grids. A  $10^\circ \times 10^\circ \times 10^\circ$  grid was used for the computation of the ODF, and the tube projection technique [43] was used to account for the low experimental pole figure coverage. Complete pole figures for both structural phases and all hkl of interest were recalculated from the ODF to facilitate the discussion of the observed orientation changes during loading / unloading. Such pole figures are internally consistent with the ODF.

For the neutron diffraction experiment on the coarse/ Ultrafined Aluminum sample, due to the limited detectors area coverage (two detectors, normal and parallel to the loading axis), only a semi-quantitative texture evolution can be represented using inverse pole figures and axial distribution plots. In an axial distribution plot the y-axis is a measure of the number of grains that are at an angle  $\phi$  between the normal to the chosen plane and the loading axis (in this case), compared to a randomly oriented polycrystal. Thus, a random polycrystalline sample would be represented by a horizontal line at

unity.

## **Results and discussion**

### Macroscopic stress-strain response

In this paragraph, the macroscopic effect of the plastic deformation in nc-UF bulk aluminum will be presented and discussed. However, before to present the results obtained from compression experiments, it is necessary to stress the importance of several items, directly correlated to the microstructure of the material. As previously described, the SPS consolidation process lead to a non-uniform microstructure in which nanocrystalline and ultrafined regions could behave differently during deformation. The grains size and the distribution of the crystallites and defects could constitute source of possible inhomogeneous strain and, consequently, different deformation mechanisms might be active during plastic deformation.

As previously described, cylindrical samples of nc-UF aluminum and coarse aluminum were plastically deformed in compression in order to investigate their postdeformation behavior. We measured the stress-strain curves for a series of deformation recovery experiment using a Baehr dilatometer with a displacement resolution of 0.5  $\mu\text{m}$ . The strain and stress resolution were 0.0005% and 5 MPa respectively.

We start describing the deformation behavior of coarse aluminum during compression up to 4% strain (Fig 31a). During loading the specimen shows the yielding around 65 MPa and a stress-strain slope in the elastic region that corresponds to 68 GPa. Following the stress-strain curve it is possible to note a strain hardening after yielding. After unloading the elastic strain is immediately recovered. The specimen was then annealed at 180°C for 10 minutes, which did not produce a significant

recovery of the plastic strain (only 0.86% of the plastic strain is recovered as shown in Fig 31b).

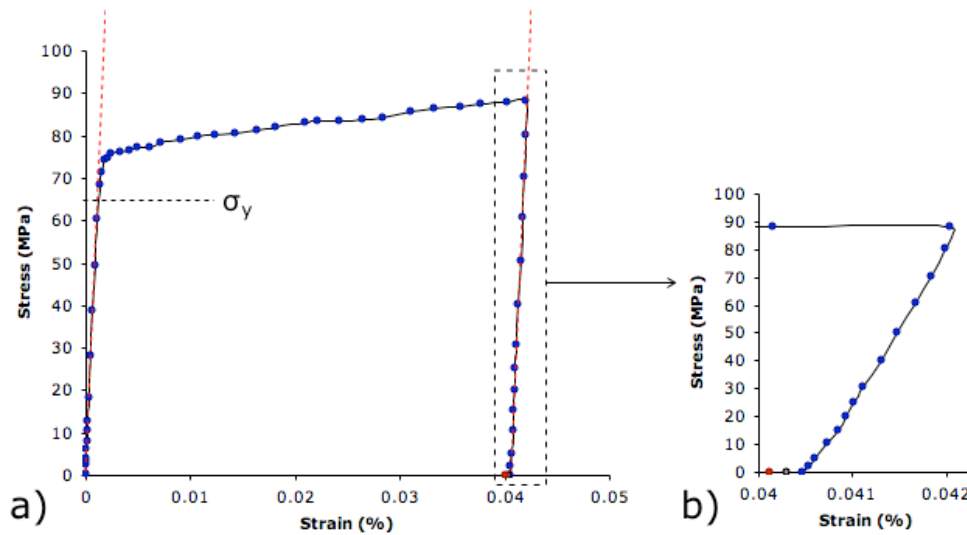


**Fig 31.** Stress-strain curve for deformation recovery experiment on coarse aluminum. The recovery was tested after 10 minutes at RT and 0 MPa and after subsequent annealing at 180°C for 10 minutes.

Time evolution of strain during RT step at 0 MPa and subsequent annealing at 180°C is shown in Fig 32. These results were used as “standard reference” in which we note that, conventional coarse aluminum of randomly oriented bulk sample as it was expected i) do not shows any recovery of plastic deformation, ii) there is a strain hardening after yielding as commonly observed in conventional metals and iii) the recovery of defects due to annealing at 180°C do not promote a significant plastic strain recovery.

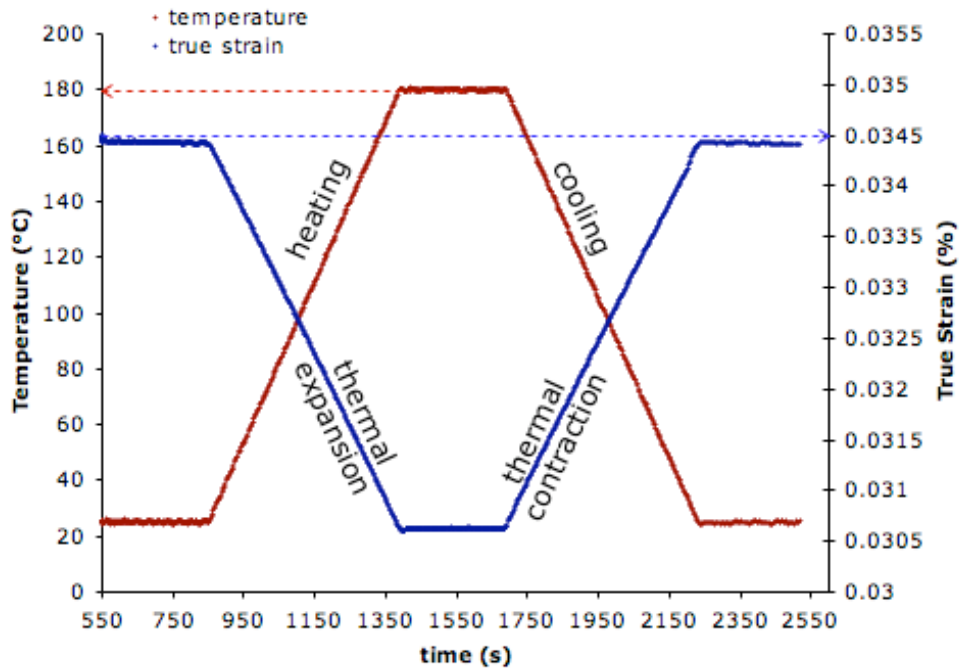


**Fig 32.** Evolution of true strain, immediately after unloading and during and after annealing at 180°C for 10 minutes. The sample (coarse Al) was deformed in compression up to 3.6% strain. No significant strain recovery was observed after the thermal cycle.

For the nc-UF bimodal bulk aluminum the loading was performed at room temperature and then the specimens were annealed at 180°C. The specimen nc\_UF Al denoted with the letter A, is referred to the first experiment in which a strain of 2.6 % (compression) was applied. During loading the specimen started yielding around 230 MPa. After compression and a total time of 400 minutes with no stress applied, the recovered plastic strain was 11 % of the total plastic deformation (Fig 33a). The behavior of the recovery (strain vs. stress) is reported in (Fig 33b). We note a sort of fluctuation of the stress always with negative values (negative values mean that the sample works along the longitudinal direction with active tensile stress).

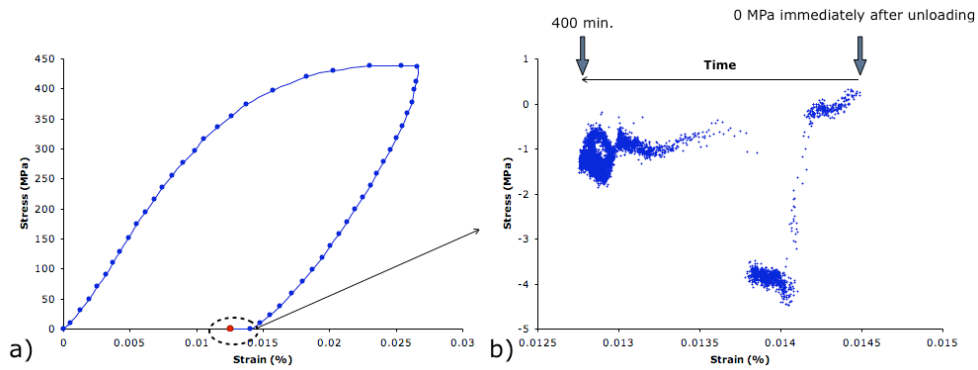


**Fig 33.** (a) Stress-strain curve for deformation recovery experiment performed on nc-UF bimodal bulk aluminum up to 2.6% of plastic strain. The sample A shows significant plastic strain recovery (11% of the total plastic strain). (b) Stress-strain curve after unloading, at 0 MPa recorded continuously for 400 minutes.

Looking the time evolution of the plastic deformation, the strain recovery at RT is time dependent (Fig 34). The results indicate that a consistent fraction of RT recovery (about 60%) occurs very quickly, within a time interval of 500 seconds. The rest of the recovery process is much slower. The recovery shown in Fig 34 can be expressed by a well known Arrhenius type law:

$$\frac{1}{\tau} = A \exp^{-Q(\epsilon_r)/RT}$$

where  $\tau$  represents the time to reach recovered strain  $\epsilon_r$  and  $Q(\epsilon_r)$  is

the activation energy.

Inset picture shows the enlarged region, documenting the recovery immediately after unloading.

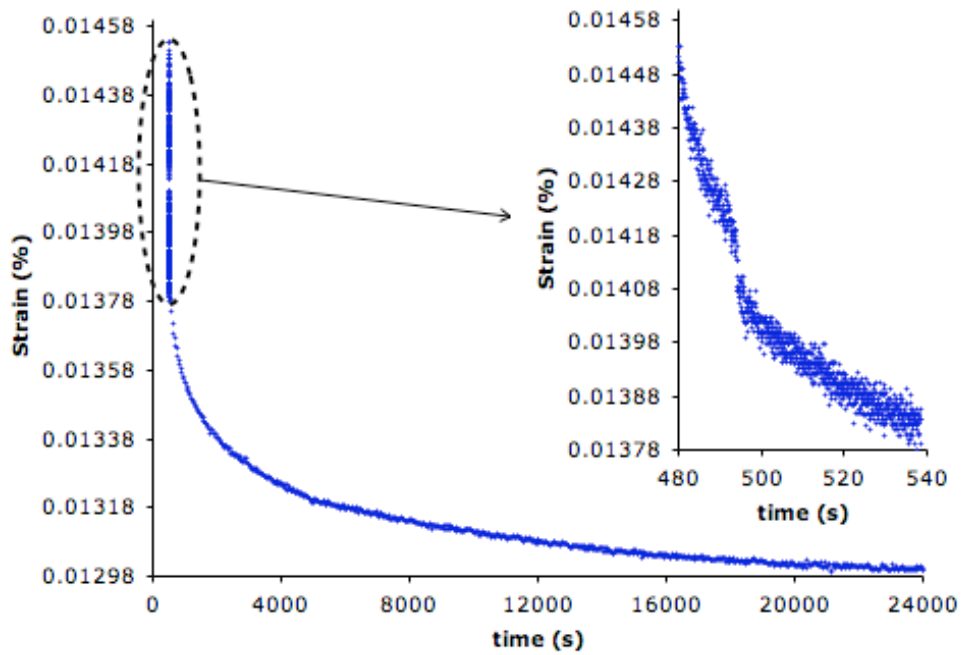


**Fig 34.** Time evolution of strain recovery at room temperature for nc-UF Al specimen A. The enlarged region (inset) documents that the majority of the recovery (60%) happens within 500 seconds.

A second specimen denoted with the letter B (prepared from the same SPS cylinder of the specimen A) was deformed in compression up to 3.6% strain (Fig 35). After compression the plastic strain recovered was around 12% of the total plastic deformation. Note that the amount of plastic strain recovery after 3.6% strain is very similar to the plastic strain recovered after 2.6% of plastic deformation.

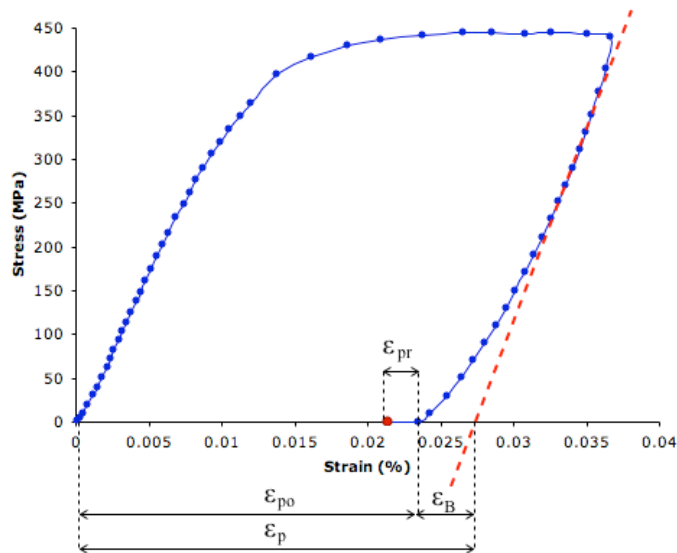


**Fig 35.** Stress strain curves for deformation recovery experiment performed on nc-UF bimodal Al specimen up to 3.6% strain (sample B). Notice the Bauschinger effect during unloading and the plastic strain recovery after unloading.

A comparison between the three stress-strain experiments presented at RT (Coarse Al Fig 31, nc\_UF\_A Fig 33 and nc\_UF\_B Fig 35) show that, for nanocrystalline samples (A and B) there is significant “self-assisted Bauschinger effect” upon unloading. Bauschinger effect could be explained as a reduction in yield stress of a material during reverse straining after being plastically deformed in the forward direction. As deformation occurs, the dislocation will propagate resulting in the formation of pile-ups and tangles. Consequently, local back stresses may be present in the material and, when the strain direction is reversed, the dislocations can move easily in the reverse direction and the yield strength of the metal becomes lower.

In this work for nanostructured aluminum samples we observed experimentally that the stress-strain response deviates from elastic

behavior during unloading, even when the samples are still under compression (Fig 33 and 35).

This behavior was observed in passivated films [44, 45] and normally been attributed to the presence of stored dislocation energy, which assist reverse plastic deformation during unloading.

To describe quantitatively the Bauschinger effect a brief description of the notation used is reported here below:

$\sigma_y$  = forward yield stress

$\sigma_{yr}$  = reverse yield stress

$\epsilon_p$  = plastic strain predicted

$\epsilon_{po}$  = plastic strain observed

$\epsilon_{pr}$  = plastic strain recovery at 0 stress applied

$\epsilon_B$  = plastic strain recovery due to the Bauschinger effect.

Analyzing the stress-strain curves, the stress-strain response reported in Fig 33 and 35 show a significant reduction in the stress-strain slope in the elastic region during loading, compared to the 68 GPa obtained from the coarse grained Aluminum (Fig 31). This behavior observed in the "elastic" region could be ascribed to the non-uniform distribution of the grain size. Large and small grains are initially subjected to deform elastically. However, during the increase of load, large grain goes into plastic deformation while nanostructured grains still deform elastically. Further increase in load leads to an increase of the volume fraction of grains that undergo to plastic deformation and a consequent reduction of grains that behave elastically. The macroscopic consequence is a sensible and continuous reduction of the stress-strain slope even at relative low stress in the as defined "elastic region". Furthermore, the apparent strain hardening observed in our specimens is most likely the manifestation of such inhomogeneous elastic-plastic deformation. To explore quantitatively the stress-strain response of nc-UF Aluminum,

several cycles of loading-unloading were performed (sample nc-UF denoted with the letter D). Figure 36 shows the stress-strain curve after five consecutive loading-unloading cycles up to 4.3% of strain.

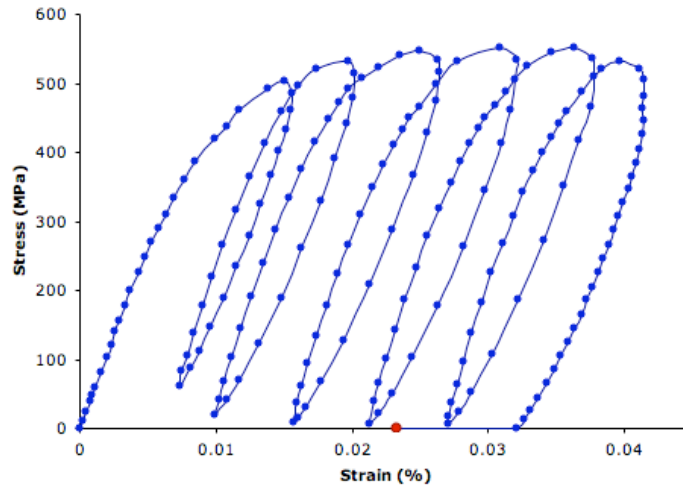


**Fig 36.** Stress-strain curves for deformation recovery experiments performed on nc-UF bimodal aluminum up to 4.3% of strain. The plastic strain recovery after unloading was about 30% of the total plastic strain.

Table 2 summarizes the results concerning the plastic strain recovered due to the Baushinger effect ( $\epsilon_B$ ), the plastic strain predicted ( $\epsilon_p$ ) if the stress-strain slope considered during loading and unloading is around 68 GPa (almost coincident with the bulk elastic modulus of aluminum) and the plastic strain recovered after unloading at 0 MPa ( $\epsilon_{pr}$ ). This constrain of the stress-strain slope is necessary in order to account as better as possible only the elastic contribution from both the big and small grains.

**Table 2.** Plastic strain recovery after unloading and due to the Baushinger effect

<b>Sample</b>	$\epsilon_p$ (%)	$\epsilon_B$ (%)	$\epsilon_{pr}$ (%)	$\epsilon_{max}$ (%)
Nc-UF (A)	1.145	0.29	0.172	2.58
Nc-UF (B)	2.239	0.31	0.237	3.62
Nc-UF (D0)	0.903	0.30	-	1.71
Nc-UF (D1)	0.613	0.28	-	2.19
Nc-UF (D2)	0.877	0.32	-	2.87
Nc-UF (D3)	0.916	0.31	-	3.36
Nc-UF (D4)	0.893	0.29	-	3.89
Nc-UF (D5)	0.842	0.30	0.781	4.33

A comparison with the different loading unloading cycles shows that the recovered strain due to the Baushinger effect  $\epsilon_B$  is almost unchanged (Table 2). More, after the first loading unloading cycle the specimen exhibited no significant residual hardening with a yield point around 260 MPa. This behavior referred to the bulk samples is similar to what described for unpassivated freestanding aluminum films but with some differences.

First, as reported also by Rajagopalan and co-workers [46] the driving force of the lost of linearity during unloading is ascribed to the inhomogeneous stress distribution stored during loading where large grains goes into plastic field early when smaller grains are still loaded elastically. In this situation, the dislocations are generated by big grains and elastic residual stress is much higher in small grains. During the initial stage of unloading we do not observe a significant apparent linearity (Fig 37 shows a loading-unloading cycle with expected and observed plastic strain) in contrast to what reported for the unpassivated freestanding Al films.

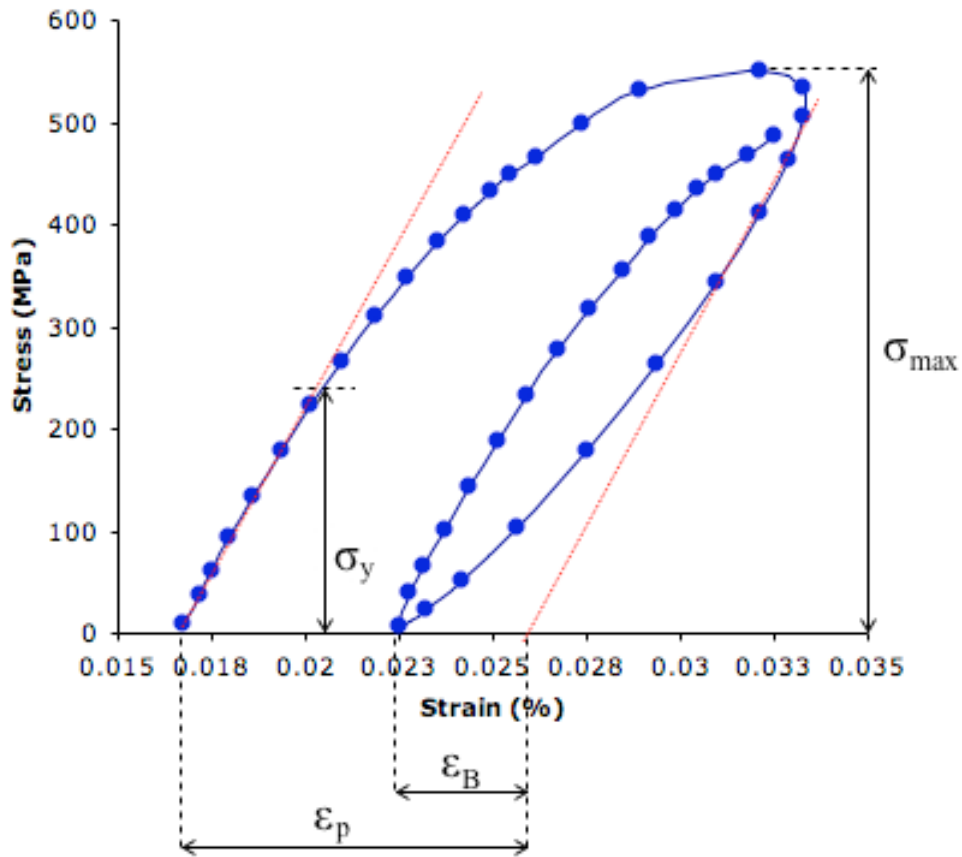


**Fig 37.** Stress-strain curves for deformation recovery experiment of sample D. Particularly, the figure displays the 4<sup>th</sup> cycle of loading-unloading (D3 in Table 2).

This particular behavior might be justified by considering an overlapping effect between grains that unload elastically and grains that must behave plastically due to local tensile stresses immediately after when unloading starts. These reversed stresses (tensile) lead to reverse plastic deformation not only in larger grains but also in the nanostructured volume fraction that must accommodate the plastic

strain of the ultra-fine volume fraction. The dislocations activity at the grain boundary might promote a sort of grain rotation particularly for nanometric grains. We will discuss later a possible mechanism in which the dislocations originated from the grain boundary can activate the grain rotation of the nanocrystalline counterpart.

Looking Fig 36 and Fig 37, the magnitude of Baushinger effect for each loading-unloading cycle was significant but almost constant ( $\epsilon_B = 0.3\%$  with an expected  $\epsilon_p = 0.9\%$  resulting in the observed plastic strain of 0.6%). But the specimen after a total strain of 4.2% with 5 cycles of loading-unloading showed a significant increase of plastic strain recovery after unloading (at 0 MPa the plastic strain recovery was about 30%) respect to the specimen deformed up to 3.6% that was able to recover only 12% of the plastic strain.

To understand a relationship between the plastic strain recovery and the effective total strain applied we performed another experiment (experiment denoted with the letter E) using the nc-UF aluminum in which the specimen was compressed up to 1.8% 2%, 3% and 4%. After each loading-unloading cycle, the specimen was maintained at 0 stress for 30 minutes, recording the amount of plastic strain recovery (Fig 38a). These consecutive deformations lead to increases in the recoverable strain up to 28% (Fig 38b) and a noticeable increase in the yield point, after the first cycle, due to work hardening (210, 310, 355 and 370 MPa).

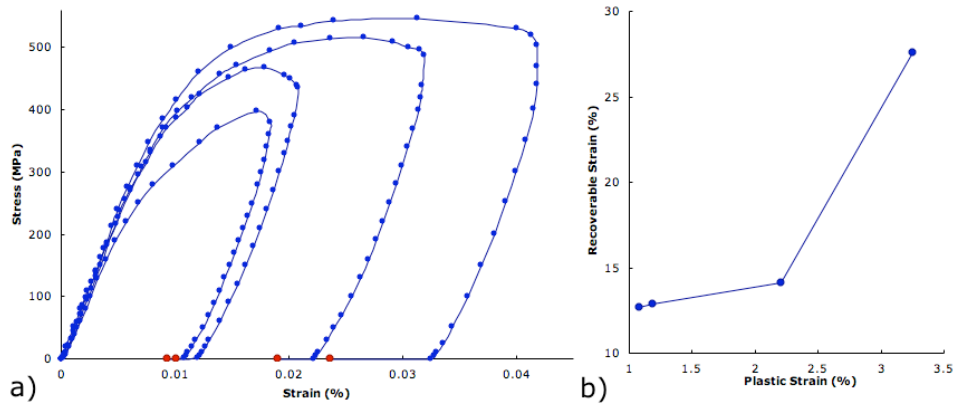


**Fig 38.** (a) Stress-strain curves for deformation recovery experiments performed on a nc-UF aluminum specimen.(b) Significant room temperature plastic strain recovery was recorded after each loading-unloading cycle.

After the last unloading followed by 30 minutes step at 0 MPa to record the plastic strain recovery at room temperature, the specimen was annealed at 180°C for 10 minutes to check for a further strain recovery. We observed a significant recovery that was quantified around 6.5% of the total plastic strain (Fig 39). Finally, the total amount of plastic strain recovered was 34.5% of the total plastic deformation. At the end, three different phenomena that promote the plastic strain recovery can be detected following the stress-strain behavior of nc-UF aluminum:

- 1) Baushinger effect during unloading that was observed in the presence of nanocrystalline-ultrafine bimodal microstructure.
- 2) Plastic strain recovery after unloading at 0 MPa and room temperature.
- 3) Plastic strain recovery after annealing at 180°C and 0 MPa.

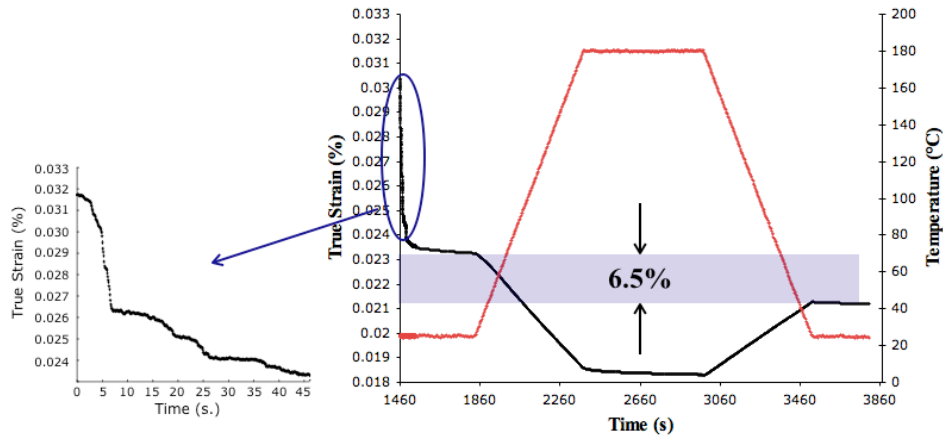


**Fig 39.** Time evolution of the strain recovery for specimen E after 4 loading unloading cycles, at room temperature with a subsequent annealing at 180°C for 10 minutes.

These observations are in partial agreement with predictions from molecular dynamic simulations, where dislocation propagation in nc-metals is hindered by grain-boundary structures such as ledges and impurities (second-phase particles) that act as the pinning points. However, our observations show that the majority of the depinning is not thermally assisted. If the inhomogeneous strain is sufficiently large, a consistent part of the plastic strain can be recovered also at room temperature. The increase in the recovery of plastic deformation may be attributed to the shear component of tensile residual stress stored after deformation in the UF grains, which acts as a driving force to glide backward dislocations. The shear component of residual stress stored in the UF grains is enhanced after further loading-unloading cycles because of the increased difference between the starting residual stress in the UF grains and the starting residual stress in the nc-grains after each cycle. From these results, in order to obtain extensive recovery of plastic

deformation, a material with a combination of UF and nc-grains is needed to generate high inhomogeneous strain and consequently high level of residual stress. This latter contribution is the driving force to overcome the energy barrier required to move dislocations back also in UF grains.

*In-situ synchrotron and neutron diffraction experiments: explaining the plastic strain recovery*

In this session we present the results of dynamics of lattice strain, microstructure and texture of bulk nanostructured aluminum sample with bimodal distribution and ultrafine-coarse sample during in-situ loading-unloading experiments. A comparison between nanostructured and coarse aluminum specimens will be presented. As previously described, the compression tests for nc-UF sample were performed on a parallelepiped (2.5x2.5x5 mm) using X-ray microfocused beam at the sector 1-ID at the Advanced Photon Source (Argonne, USA), whilst for bulk coarse aluminum in-situ neutron diffraction technique (Los Alamos Neutron Science Center) was used to have good statistics even with big grain size (cylinder of 10 mm diameter and 25 mm length and a beam size of 10 mm). Fig. 40 provides experimental evidence that grain refinement occurred for nc-UF aluminum during the in situ synchrotron compression test. Bright field (BF) and dark field (DF) TEM pictures indicate the presence of nano-sized grains ranging between 40 and 120 nm. This size distribution as well as the relevant volume fraction of UF grains (about 40%), are considered in the following discussion.

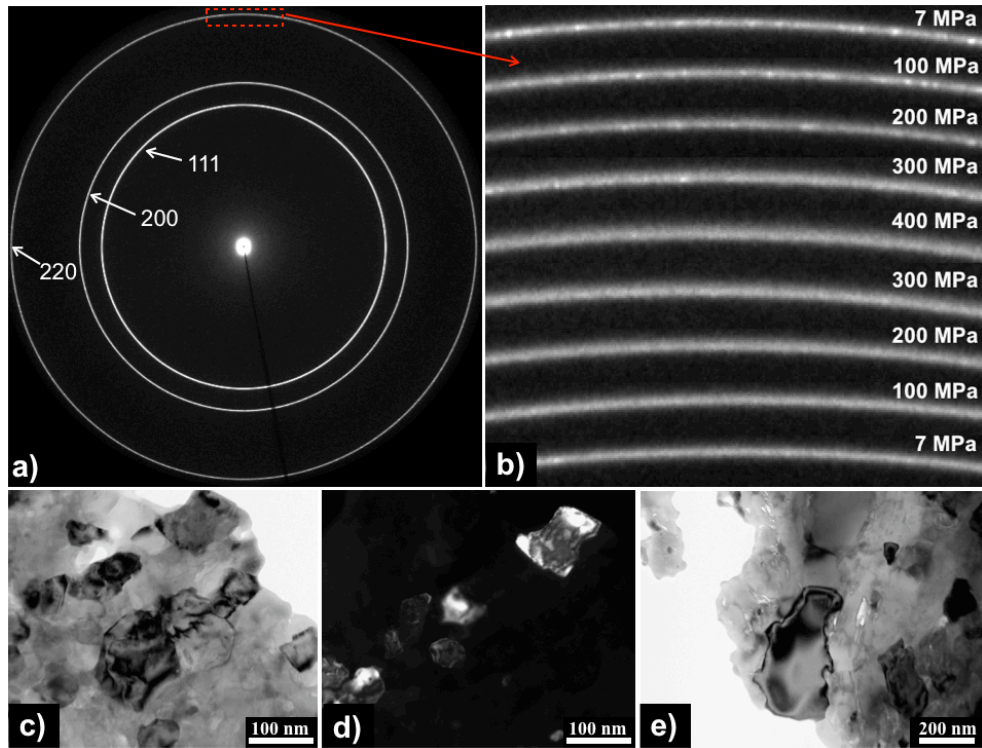


**Fig 40.** (a) One full 2D diffraction pattern obtained from the image plate detector during applied load. (b) Enlarged image of the 10° sector of the 220 Debye ring collected during loading-unloading experiment at different stress applied. Bright spots are representative to the scattering from relatively large grains (around 400 nm). During loading, these spots change their azimuthal position (grain rotation) and finally disappear (grain refinement). (c) Bright field TEM image shows the spread of the grain size distribution in the nanostructured volume fraction. (D) Dark field of C. (E) Bright field TEM image shows some ultrafine grains.

The sample was loaded in 100 MPa steps to 400 MPa, and then unloaded, with diffraction data collected for 30 sec at every 100 MPa interval. After each stress/strain increment the 2D diffracted pattern, representative to the 3D diffracted volume, was recorded (Fig 40a). Fig

40b shows a magnified portion of the (220) Debye-Sherrer ring ( $10^\circ$  sector along compression direction) as a function of load. Several spots are present in the undeformed state, which are attributed to relatively large UF grains, which are nevertheless always smaller than 500 nm (Fig 40c, d and e). Under applied stress, several features can be qualitatively recognized from the figure.

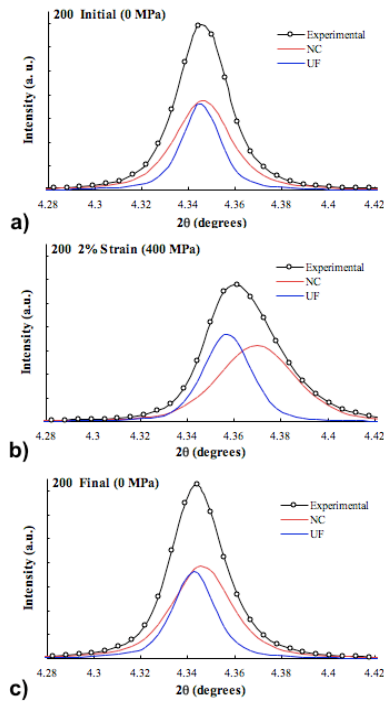
First, from 7 to 100 MPa some diffracted spots change their position and intensity along the Debye rings. This is ascribed to the fact that during compression the illuminated volume, and thus grain population, changes slightly. In addition, under applied stress, even below 100 MPa, dislocation-based plasticity can promote the formation of cells and subgrains in the UF volume fraction, leading to a grain refinement and grain rotation.

Second, from 200 MPa up to 400 MPa, the size of the spots decreases, indicating a dramatic grain refinement. Watching the UF grains behavior we argue that, during plastic strain, extensive dislocation activity might promote formation of walls and dislocation free regions with low angle grain boundaries ( $1^\circ$ - $2^\circ$ ). The mechanism is similar to that experimentally observed by Jakobsen and co-workers [29] in which, inside of single grains, they report a sort of splitting of dislocations-free regions into two regions with different orientations. In contrast, recent studies on in-situ TEM observations in load nanocrystalline aluminum films [47] have shown a fast grain boundary motion and grain growth near to the most highly stressed regions (eg. at the crack tip). However, subgrains with low mismatch angles are not sensitive to TEM inspections, so that such observations are biased to reveal only high angle grain boundary motions [48]. Moreover, the experiments reported above describe the deformation mechanism in thin electrodeposited films in which the ratio between free surface and grain boundary volume fraction is very high compared to what happen in bulk material.

Third, during and after unloading, we observe a recovery of the peak broadening. As shown in our recent work [49], this is attributed to the recombination of partial and full dislocations within the nanocrystalline volume fraction, primarily in the vicinity of grain boundaries.

As described in the previous paragraph, the mechanical behavior is governed by the inhomogeneous strains (formed during loading that are the principal sources of inhomogeneous residual stress). This behavior is mainly due to the broad grain size distribution and to the consequent inhomogeneous interaction between UF and nc grains. Inhomogeneous strains act as a backstress to drive the dislocations back to the grain boundaries where they originate.

To support this scenario, recent results reported earlier [12], [47] show dislocation activity as the primary deformation mechanism, even in nc grains. To properly characterize the material response during loading, we treat the nc and UF volume fractions as two distinct phases, with correspondingly distinct lattice strains, textures and microstructures (crystallite size and microstrain). Fig 41a, b and c show the 200 diffraction peaks, parallel to the loading axis, before, during and after an applied stress of 400 MPa.



Deconvolution of experimental asymmetric peak profile into two symmetric peaks with Rietveld analysis



- Distinct peak breaths (grain sizes and microstrains)
- Distinct volume fraction
- Distinct internal stresses
- Crystallographic texture

**Fig 41.** (a) Deconvolution into nc and UF contribution of the 200 peak profile along the loading direction when pre-load (7 MPa) is applied. (b) Deconvolution of the 200 peak at 400 MPa and 2% strain. (c) Deconvolution after loading-unloading cycle.

The experimental peak (black dotted line) can be described as the convolution of two symmetric peaks, representative of the nc and UF contributions (blue and red line respectively). Using combined Rietveld, stress, texture and microstructure analyses we can follow the dynamics of the deformation process, during the entire loading-unloading cycle. Dislocation activity, inhomogeneous local strains and stresses lead to a dynamic rearrangement of the shape of nano-sized grains [47] and this can in principle generate a reorientation of grains. These three insights have to be interconnected and explained in term of deformation mechanism (dislocation assisted), interaction between ultrafine and

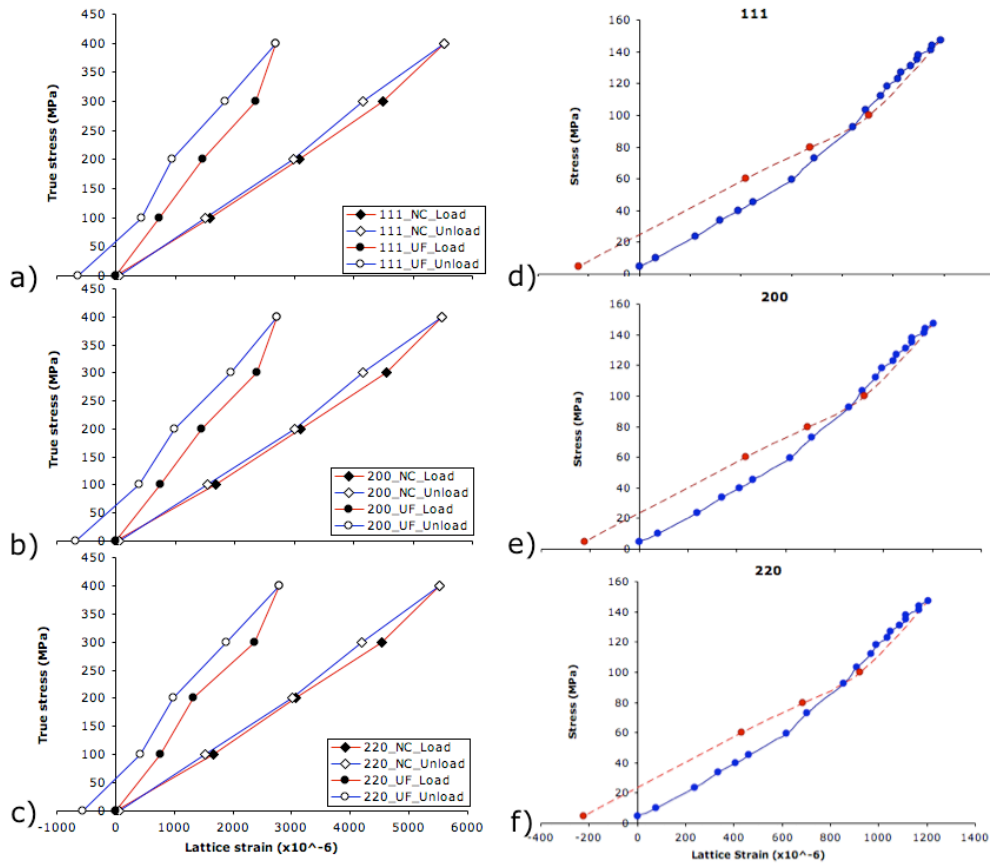
nano-crystalline grains and dislocation recovery after unloading.

Fig 42 a, b and c show lattice strain of 111, 200 and 220 reflections parallel to the loading direction as a function of applied stress. The lattice strain  $\varepsilon^{hkl}$  is calculated using the following equation:

$$\varepsilon^{hkl} = (d^{hkl} - d_0^{hkl}) / d_0^{hkl}$$

where  $d_0^{hkl}$  is the peak position in the pre-load state.

The deconvolution of the experimental profile in two distinct entities (Fig 41), allow us to treat separately the nc and UF volume fractions to study first the lattice strain interactions along the loading-unloading cycle. Coarse aluminum specimen analyzed using neutron diffraction was deformed in compression up to 9.5% strain and Fig 42 d, e and f show the corresponding lattice strain of 111, 200 and 220 reflections. Even for coarse monomodal grain size we observe a residual lattice strain but smaller and only after an extensive plastic deformation.



**Fig 42.** (a) The lattice strain evolutions of the 111, (b) 200 and, (c), 220 reflections as a function of applied stress of the nc-UF bimodal Al sample obtained using high energy synchrotron diffraction. The deconvolution approach shows the lattice strain contributions from the nc and UF counterpart. (d) The lattice strain evolution of the 111, (e) 200 and, (f) 220 reflections as a function of applied stress of the coarse Al obtained using neutron diffraction.

Fig 43 shows a comparison between lattice strain of nc-UF aluminum (a) and coarse aluminum (b) using the same scale.

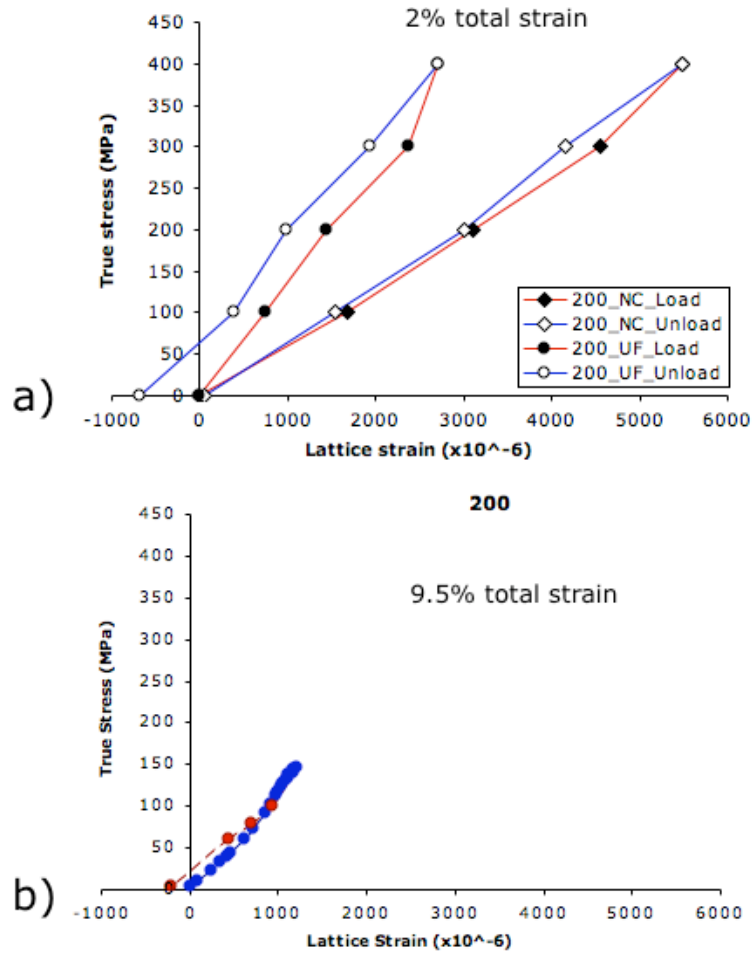


**Fig 43.** Comparison of lattice strain between nc-UF bimodal Al and coarse Al, using the same scale.

Here, it should be noted that UF grains behave as a coarse grained Al, with Frank-Read sources and dislocation pile-up as active deformation mechanisms, while the nc matrix deforms in a single dislocation regime, with an enhanced elastic limit [26]. Describing the evolution during loading, at 100 MPa under compression we observe immediately a

splitting due to the different elastic-plastic behaviors generated as a consequence of the interaction between big grains, which start to deform plastically while the nc matrix continues to deform elastically. As a result, the applied load is partitioned between grains with strongly different levels of plastic deformation. In Fig42, considering the UF volume fraction, the lattice strain deviation of the 111, 200 and 220 from the elastic linearity is appreciable above 100 MPa. As reported by Li and co-workers [50] in a random distributed single-phase material with a monomodal grain size distribution, when plastic deformation starts, dislocation slip operates first for grain whose slip system is oriented along the strain axis, while other grains not favorably oriented continue to deform elastically. As a result, the applied load (tensile test for Li and co-workers) is partitioned to the grain sets that have not plastically deformed yet. The effect observed in the paper cited above is that grain family that deforms plastically shows a compressive shift (called upward inflection), whilst grain family like {200} that stays elastic the longest, carries more load after plastic deformation and, thus, exhibited a tensile shift (called downward inflection). It is relevant to mention that the experiment reported above was done on nc and coarse Ni that have a quite high elastic anisotropy along different hkl directions. Here, aluminum is almost isotropic in terms of elasticity and the main features are more unambiguously related to a bimodal microstructure and correspondingly different deformation mechanisms acting simultaneously during loading-unloading experiment. As a result for both nc-UF aluminum and coarse aluminum, all the considered orientations (111, 200 and 220) show an upward inflection that means in our case a tensile shift (Fig 42).

The lattice strains corresponding to the nc volume fraction show a linear relationship with applied stress up to 300 MPa. Between 300 and 400 MPa generalized plastic phenomena are active in both in the nc and UF

microstructure. After unloading the residual tensile lattice strain in the UF grains is the direct consequence of the elastic behavior observed and the need to preserve the stress equilibrium between neighboring grains. Following the lattice strain evolution approach, the plastic behavior may be understood by watching the dynamics of the dislocations in UF and NC volume fractions, during the loading-unloading cycle. Molecular dynamic simulation have recently shown that the fcc metals with an average grain size of 100 nm, display a strong affinity to form full dislocations from trailing partials instead of twins [51]. These results are in good agreement with the microstructure observed by TEM after 4% strain (Fig 44 a-d).

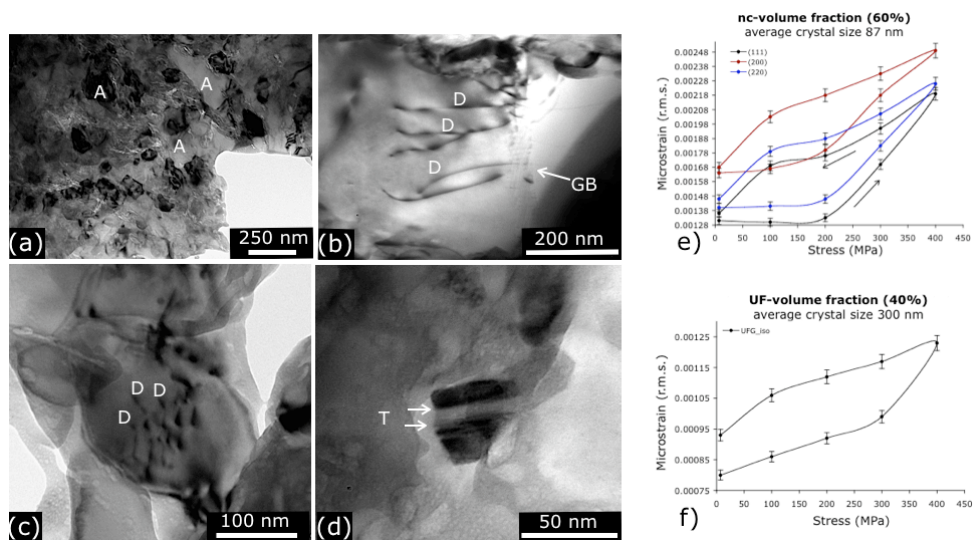


**Fig 44.** Bright-field (BF) TEM images after 2% strain: (a) BF TEM image shows a bimodal microstructure where some UF grains were marked with the letter A. (b) Dislocation lines in a relatively large grain (average around 380 nm). (c) Still complete extended dislocations in an equiaxed grain (average size around 150 nm). Twinning and, probably, stacking faults in a nc-grain (average size 40 nm). (e) and (f) show the evolution of microstrain of nanocrystalline and ultrafine fractions during loading-unloading.

Post mortem TEM inspection shows only the presence of very few grains that were able to twin after deformation. Moreover, as previously mentioned we observed a full recovery of dislocation after unloading, particularly in nc volume fraction (Fig 44 e, f), and a significant macroscopic plastic strain recovery.

This means that dislocation nucleation from grain boundaries plays a key role in the deformation behavior even in nc grains.

In this line, dislocations induce local rotations of the lattice plane, promoting lattice preferred orientation (LPO) that, if quantified, can in principle be used to evaluate the type and the entity of the plastic strain.

Connecting the dynamics of dislocations and the lattice preferred orientation development, we can also describe the annihilation of dislocations during and after unloading. To do this, the full X-ray diffraction images collected at each applied stress, during loading-unloading cycle were analyzed using the Rietveld method, determining the orientation distribution function (ODF) with the tomography algorithm EWIMV that allows data to be entered at arbitrary pole figure positions [42].

Fig 45 shows the evolution of the texture in the nc-UF aluminum specimen calculated during loading-unloading experiment. The 111, 200 and 220 pole figures are reported instead of the ODF (the pole figures are the 2D projections on the selected plane of the 3D ODF). The starting texture is nearly random as expected after the SPS consolidation process. At 100 MPa the texture is still randomly distributed as shown in Fig 46, where the plot of the 111 pole figure intensity (multiplies of random distribution) versus applied load is reported. From 200 MPa to 400 MPa we observe a detectable and coherent texture with two main components, 111 and 200, parallel to the compression direction.

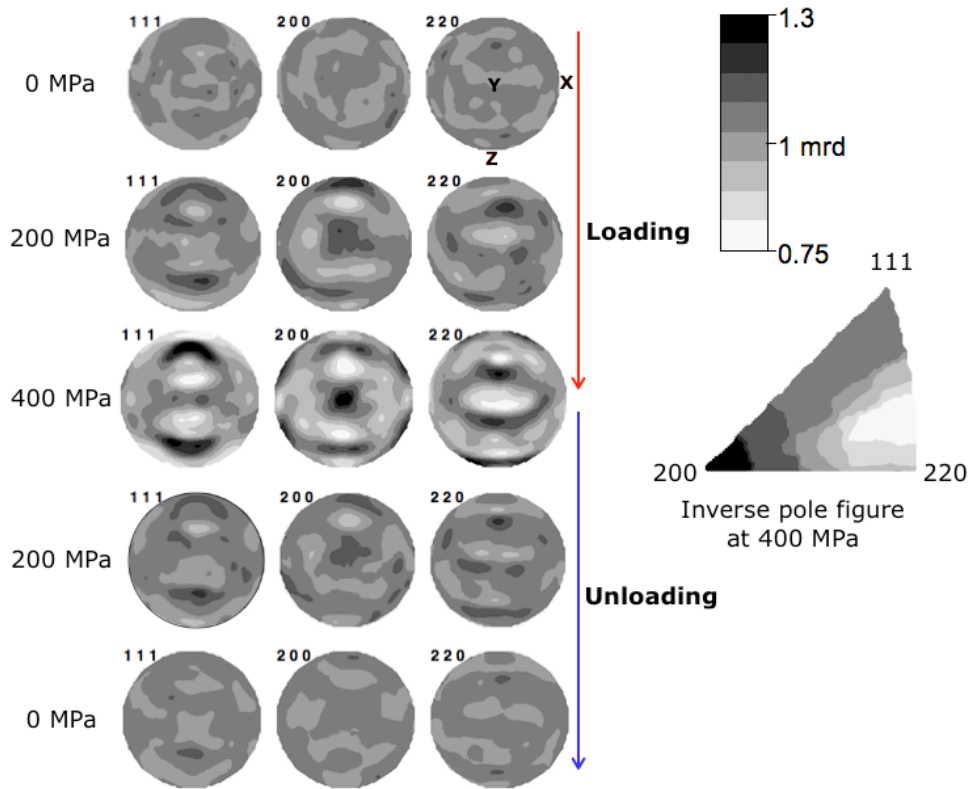


**Fig 45.** 111, 200 and 220 pole figures calculated using Rietveld method and EWIMV algorithm along the entire loading-unloading cycle in nc volume fraction. Shear texture shows recovery after unloading. The inverse pole figure shows very clear a 200 texture component developed during loading.

In this case the normal direction denoted with the letter Y, (the center of the pole figures) corresponds to the loading direction. We note that

there is a development of the 200 texture component, parallel to the loading axis.

During and after unloading the texture recover, resembling a randomly distributed orientation.

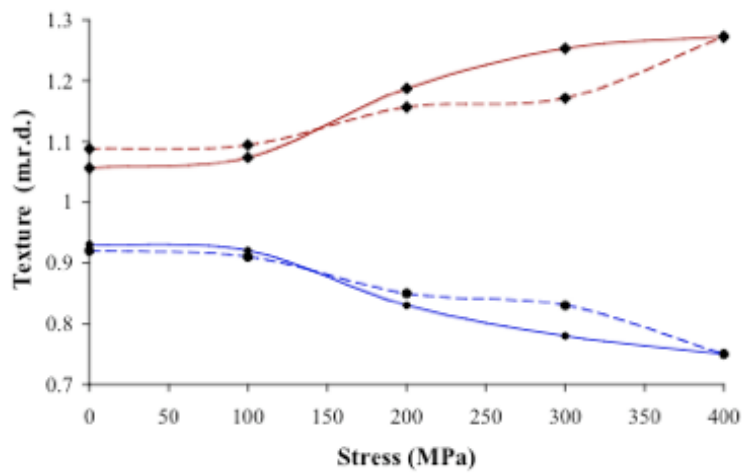


**Fig 46.** 111 texture changes along the loading-unloading cycle. Intensity of texture is measured in multiples of random distribution

These results are in good agreement with the TEM observations and molecular dynamic simulations reported earlier in which, fcc metals with high stacking fault energies (eg. Al) deform by dislocation movement even in nano-sized grains. During and after unloading the texture in both nc and UF volume fractions is almost completely reversed. We note that the texture recovery is characterized by a two-step evolution, as shown in Fig 46.

A possible explanation could be summarized as follow:

during propagation, dislocations can become temporarily pinned at GB

ledge structures and their associated stress intensities, and upon depinning (due to inhomogeneous local strains that increase during unloading) they propagate further on the slip plane in which the dislocation had originally nucleated. As a possible consequence, grain rotation takes place. We argue that the driving force for the texture recovery and dislocation recombination, as well as plastic strain recovery that can be macroscopically observed only after unloading, can be ascribed to the inhomogeneous lattice strains induced by the bimodality of the microstructure.

To corroborate these assumptions, the lattice preferred orientation developed during compression on coarse aluminum specimen is reported in Fig 47. Due to the diffraction geometry discussed in a previous section, we report the inverse pole figures that describe a development of a preferred orientation along 220 during loading.

During unloading the texture remains unchanged.

These results may constitute the basis for a future work in which plastic strain recovery will be tested for others materials trying to understand in details the relationship between microstructure and plastic strain recovery related phenomena.

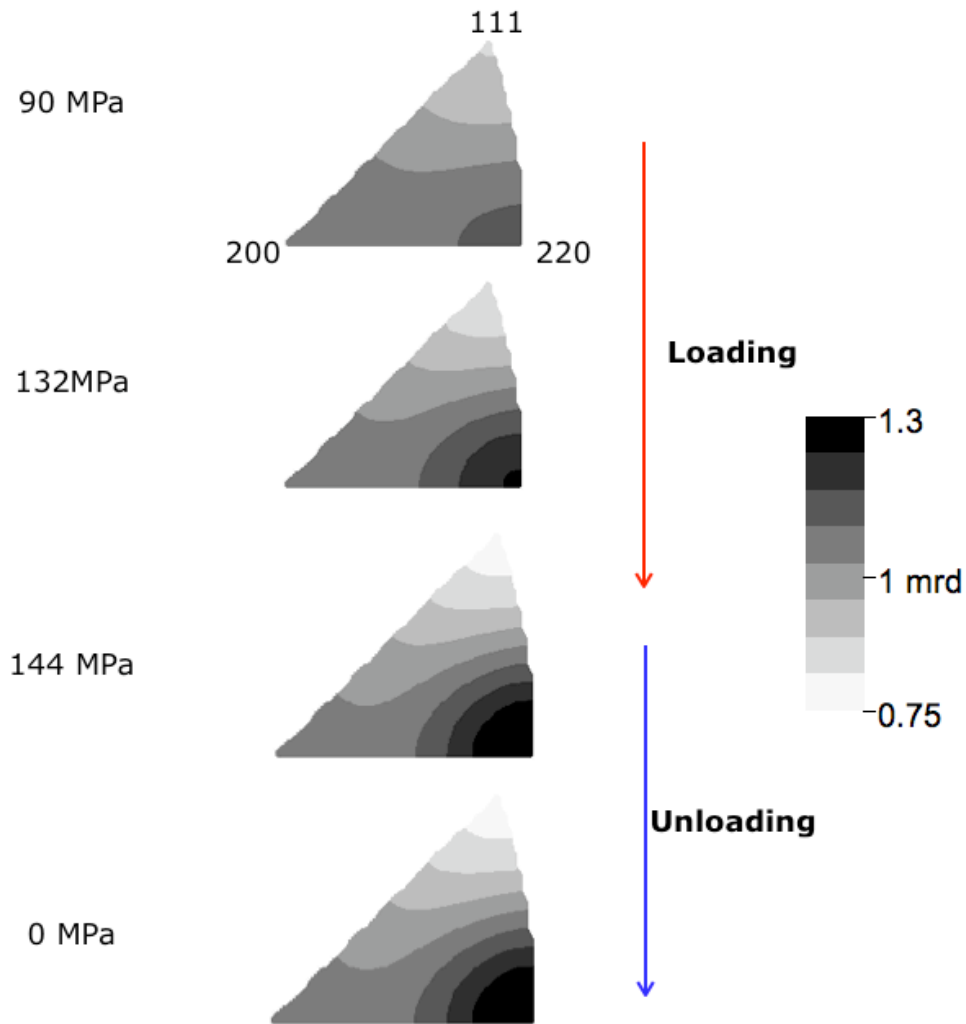


**Fig 47.** Inverse pole figures of coarse Al calculated using data collected along loading direction during loading-unloading experiment. The texture developed at 9.5% strain remains unchanged after unloading.

## **Summary**

In this chapter we have analyzed the plastic strain recovery in a bimodal nc-UF Al system using Baehr dilatometer configured for compression test. The results described here indicate that a consistent part of the plastic strain can be recovered after unloading (about 40% of the total plastic strain) by three distinct phenomena: Baushinger effect during unloading, plastic strain recovery at RT after unloading and plastic strain recovery during annealing without any stress applied. There are in literature studies that report Baushinger effect during unloading only in thin films but no previous reports on bulk samples. Here, the results show unambiguously that nanocrystalline-ultrafine bulk aluminum samples exhibit Baushinger effect. This means that as a consequence of different behavior during loading between nanostructured grains and ultrafined grains, there is a generation of high inhomogeneous strains and high residual stress that act as driving force for a development of the Baushinger effect even at the early stage of unloading. Selective plastic relaxation of larger/favorably oriented grains, coupled with elastic accommodation in smaller/unfavorably oriented grains and other deformation-related phenomena (grain boundary activity, grain rotation and sliding etc.), appears to be the explanation.

But the Baushinger effect is just the first step of the recovery and was observed to be independent to the amount of the plastic strain. After unloading, the internal stresses may not fully relax during unloading and a consistent part of recovery occurred after unloading. Again, the recoverable part of the deformation depends on the internal stresses accumulated and should have a maximum that is proportional to the grain size distribution and to the extent of plastic deformation. Above this limit plastic deformation would be expected to occur without any possibility of recovery. Residual dislocations pinned by grain boundary structures like ledges or by second-phase particles during propagation,

require thermal activation to depin and propagate further but the recovery of plastic strain associated to the annealing is the minor part. Using in-situ synchrotron and neutron diffraction experiments the nc-UF and coarse aluminum samples were dynamically characterized in terms of microstructural changes (evolution of microstructure, residual lattice strain and texture).

### References

- [1] E.O. Hall Phys Soc Lond B 64 (1951) 747.
- [2] N.J. Petch, J Iron Steel Inst 174 (1953) 25.
- [3] R.A. Masumura, P.M. Hazzledine, C.S. Pande, Acta Mater 46 (1998) 4527.
- [4] A. Chokshi, A. Rosen, J. Karch, H. Gleiter, Scripta Metall 23 (1998) 1679.
- [5] C. Cheung, F. Djuanda, U. Erb, G. Palombo, Nanostruct Mater 5 (1990) 513.
- [6] D. Gruen Annu Rev Mater Sci 29 (1999) 21.
- [7] M. Jin, A. M. Minor, E. A. Stach, J. W. Morris Jr., Acta Mater. 52 (2004) 5381.
- [8] M. Jin, A. M. Minor, J. W. Morris Jr., Thin Solid Films 515 (2007) 3202.
- [9] K. Zhang, J. R. Weertman, J. A. Eastman, Appl. Phys. Lett. 87 (2005) 061921.
- [10] D. Pan, S. Kuwano, T. Fujita, M.W. Chen, Nano Lett. 7 (2007) 2108.
- [11] S. Brandstetter, K. Zhang, A. Escudro, J. Weertman, H. Van Swygenhoven, Scr. Mater. 58 (2008) 61.

- [12] D.S. Gianola, S. Van Petegem, M. Lagros, S. Brandstetter, H. Van Swygenhoven, K.J. Hemker, *Acta Mater.* 54 (2006) 2253.
- [13] CH Li, E H Edwards, J Washburn, ER Parker, *Acta Metall* 1 (1953) 223.
- [14] DW Bainbridge, CH Li, EH Edwards, *Acta Metall* 2 (1954) 322.
- [15] TJ Rupert, DS Gianola, Y Gan, KJ Hemker, *Science* 326 (2009) 1686.
- [16] JW Cahn, Y Mishin, A Suzuki, *Acta Mater* 54 (2006) 4953.
- [17] VA Ivanov, Y Mishin, *Phys. Rev. B* 78 (2008) 064106.
- [18] J W Cahn, J E Taylor, *Acta Mater* 52, 4887 (2004).
- [19] Z. Shan, E.A. Stach, J.M.K. Wiezorek, J.A. Knapp, D.M. Follstaedt, S.X. Mao, *Science* 305 (2004)654.
- [20] N Q Vo, R S Averback, P Bellon, S Odunuga, *A Caro Phys. Rev. B*, 77 (2008) 134108.
- [21] V Yamakov, D. Wolf, S R Phillpot, A K Mukherjee, H Gleiter, *Nature Materials* 3 (2004) 43.
- [22] J Schiotz, K W Jacobsen, *Science* 301 (2003) 1357.
- [23] H Van Swygenhoven, P M Derlet, A Hasnaoui, *Physical Review B* 66 (2002) 024101.
- [24] J Rajagopalan, JH Han, M T A Saif, *Science* 315 (2007) 1831.
- [25] Z Budrovic, H Van Swygenhoven, P M Derlet, S V Petegem, B Schmitt, *Science* 304 (2004) 273.
- [26] L. Thilly, PO Renault, V Vidal, F Lecouturier, S Van Petegem, U Stuhr, H Van Swygenhoven, *Appl. Phys. Lett.* 88 (2006) 191906.
- [27] TS Han, PR Dawson, *Mater. Sci. Eng. A* 405 (2005) 18.
- [28] I Lonardelli, HR Wenk, L Lutterotti, M Goodwin *J. Synchrotron Rad.* 12 (2005) 354.

- [29] B Jakobsen, H F Poulsen, U Lienert, J Almer, SD Shastri, HO Sorensen, C Gundlach, W Pantleon, *Science*, 312, (2006) 889.
- [30] I Lonardelli, N Gey, HR Wenk, M Humbert, SC Vogel, L Lutterotti, *Acta Mater*, 55 (2007) 5718.
- [31] AP Hammersley, SO Svensson, A Thompson, *Nucl Ins. Meth. A346* (1994) 312.
- [32] MAM Bourke, DCE Dunand, E Ustundag, *Appl Phys A* 74 (2002) S1707.
- [33] HR Wenk, L Lutterotti, S. Grigull, S Vogel, *Nucl Instrum Methods A* 515 (2003) 575.
- [34] HM Rietveld, *J Appl Cryst* 2 (1969) 65.
- [35] L Lutterotti, S Matthies, HR Wenk, AS Shultz, JW Richardson, *J Appl Phys* 81 (1997) 594.
- [36] MAUD package: <http://www.ing.unitn.it/~maud/>
- [37] HM Rietveld, *Acta Crystallogr.* 20 (1966) 508.
- [38] HM Rietveld, *Acta Crystallogr.* 21 (1966) A228.
- [39] R A Young (Ed.), *The Rietveld Method*, Oxford University Press, 1995.
- [40] NC Popa, *J Appl Cryst* 31 (1998) 176.
- [41] Tomè CN, Canova GR In: Kocks UF, Tomé CN, Wenk H-R editors. *Texture and Anisotropy: preferred orientation in polycrystals and their effect on materials properties.* 2<sup>nd</sup> ed. Cambridge: Cambridge University Press; 2000. P. 466.
- [42] S. Matthies, G.W. Vinel. *Phys. Stat Solidi (b)* 112 (1982) K111.
- [43] K. Pawlik, *Phys Stat Solidi (b)* 134 (1986) 477.
- [44] R P Vinci, SA Forrest, JC Bravman, *J. Mater Res* 17 (2002) 1863.
- [45] S P Baker, R M Keller-Flaig, J B Shu, *Acta Mater.* 51 (2003) 3019.

- [46] J Rajagopalan, J H Han and M T A Saif, *Scripta Mater* 59 (2008) 734.
- [47] M. Lagros, D.S. Gianola, K.J. Hemker, *Acta Mater* 56 (2008) 3380.
- [48] Y. Zhong, D. Ping, X. Song, F. Yin, *J. Alloys Compd* 431 (2009) 433.
- [49] I Lonardelli, J Almer, G Ischia; C Menapace, A Molinari, *Scripta Mater* 60, (2009) 520.
- [50] H. Li, H. Choo, Y. Ren, T.A. Saleh, U. Lienert, P.K. Liaw, F. Ebrahimi, *Phys Rev Lett* 101 (2008) 015502.
- [51] D.H. Warner, W.A. Curtin, S. Qu, *Nature Mat.* 6 (2007) 876.

## **Conclusions**

This PhD thesis had as main objective to study the plastic deformation behavior in bulk nanocrystalline/ultrafine aluminum obtained by cryomilling and Spark Plasma Sintering of powders.

In chapter 1 we showed how a nanostructured Al powder can be obtained and how the study of the structural characteristics of the different granulometric fractions of the cryomilled Al powder may give an insight of the kinetics of the milling. The crystallite size and the microstrain in the cryomilled powder investigated cover a broad range: the finer the particle size, the finer the crystallite size and the larger the microstrain. This is expected to have noticeable effect on the thermal stability of the nanostructured material, since the thermodynamic driving force depends on the specific grain boundary surface area, and the lattice strain offers a resistance to the grain boundary mobility during grain growth. However, additional phenomena concur to define the thermal stability of nanostructured Al obtained by cryomilling, as the drag stress exerted by grain boundary impurities, second phase particles and nanopores.

In the second chapter, Spark Plasma Sintering consolidation process was presented. Based on the results of the thermal stability study described in chapter 1, full dense bulk nanostructured Al samples were produced via SPS. To achieve the desired samples densification, we proposed a sintering methodology in which the cryomilled powder was degassed in situ in order to avoid expensive and time consuming heat treatments in high vacuum and prevent also the grain growth of the unsintered powder. Bulk Al samples produced via SPS have shown a bimodal microstructure where nanostructured and ultrafine regions are both present, interacting each others.

Finally, chapter 3 was dedicated to the main goal of this PhD thesis:

study of deformation mechanism and plastic strain recovery in bulk bimodal nc-UF aluminum. The conclusions can be summarized as follow:

1) The macroscopic stress-strain behavior showed a detectable "self-Bauschinger effect" during unloading when the sample was still in compression. This can be ascribed to the inhomogeneous lattice strain due to the different deformation behavior between nanocrystalline and ultrafine counterpart.

2) After unloading, there is a significant part of the plastic strain that can recover. The recoverable part of the deformation depends on the internal stresses generated by inhomogeneous strain and should have a maximum that is proportional to the grain size distribution and to the extent of plastic deformation.

3) The residual tensile lattice strain is the driving force to a recovery of plastic strain that is the consequence of the recovery of dislocations after unloading. We observed a further 6% of plastic strain recovery after annealing at 180°C.

4) The recovery of dislocations seems to promote local rotation during unloading. As a consequence the driving force for the observed texture recovery and dislocation recombination is the inhomogeneous lattice strain induced by the bimodal microstructure.

5) No plastic strain recovery was observed in coarse monomodal Al even for "high levels" of plastic strain (9.5%).

6) Dynamic evolution of texture can be used as an indicator of

the recovery of the plastic deformation.

These insights constitute a natural bridge between plastic strain recovery, texture recovery and dislocation recombination. This could contribute to stimulate further research on fundamental deformation mechanisms, especially for taking into account interaction between different grain size distributions.

## **Publications**

- [1] HR Wenk, I. Lonardelli, D. Williams. Texture changes in the hcp-bcc-hcp transformation on Zr studied in situ by neutron diffraction. **Acta Materialia**, **52 (2004) 1899**.
  
- [2] HR Wenk, I. Lonardelli, J. Pehl, J. Devine, V. Prakapenka, G. Sen, HK Mao. In situ observation of texture development in Olivine, Ringwoodite, Magnesio-wustite and silicate Perovskite at High Pressure. **Earth and Planetary Science Letter**, **226 (2004) 507**.
  
- [3] I. Lonardelli, HR Wenk, L. Lutterotti, M. Goodwin. Texture analysis from synchrotron diffraction images with the Rietveld method: Dinosaur tendon and Salmon scale. **Journal of Synchrotron Radiation**, **12 (2005), 354**.
  
- [4] HR Wenk, I. Lonardelli, SC Vogel, J. Tullis. Dauphiné twinning as evidence for an impact origin of Preferred orientation in quartzite: an example from Vredefort, South Africa. **Geology**, **33 (2005), 273**.
  
- [5] HR Wenk, I. Lonardelli, E. Rybacki, G. Dresen, N. Barton, H. Franz, G. Gonzales. Dauphiné twinning and texture memory in Polycrystalline Quartz. Part 1: Experimental Deformation of Novaculite. **Physics and Chemistry of Mineral** **33 (2006), 667**.
  
- [6] S. Speziale, I. Lonardelli, L. Miyagi, J. Pehl, CE Tommaseo, HR Wenk. Deformation experiments in the diamond-anvil cell:

texture in copper to 30 GPa. **Journal of Physics Condensed Matter 18 (2006) 1.**

- [7] HR Wenk, I. Lonardelli, S. Merkel, L. Miyagi, J. Pehl, S. Speziale, CE Tommaseo. Deformation textures in diamond anvil experiments, analyzed in radial diffraction geometry. **Journal of Physics Condensed Matter 18 (2006) 16.**
  
- [8] HR Wenk, I. Lonardelli, H. Franz, K. Nihei, S. Nakagawa. Preferred orientation and elastic anisotropy of illite clay. **Geophysics 72 (2007) E69.**
  
- [9] I. Lonardelli, HR Wenk, Y. Ren. Preferred orientation and elastic anisotropy in shales. **Geophysics 72 (2007) D33.**
  
- [10] I. Lonardelli, N. Gey, HR Wenk, M. Humbert, SC Vogel, L. Lutterotti. In situ observation of texture evolution during  $\alpha$ - $\beta$  and  $\beta$ - $\alpha$  phase transformations in Titanium alloys investigated by neutron diffraction. **Acta Materialia 55 (2007) 5718.**
  
- [11] J. Gomez Barreiro, I. Lonardelli, HR Wenk, G. Dresen, E. Rybacki, Y. Ren, CN Tomé. Preferred orientation of anorthite deformed experimentally in Newtonian creep. **Earth and Planetary Science Letter 264 (2007) 188.**
  
- [12] S. Gialanella, F. Deflorian, F. Girardi, I. Lonardelli, S. Rossi. Kinetics and microstructural aspects of the allotropic transition in tin. **Journal of Alloys and Compounds 474 (2009) 134.**

- [13] A. Glage, R. Ceccato, I. Lonardelli, F. Girardi, F. Agresti, G. Principi, A. Molinari, S. Gialanella. A powder metallurgy approach for the production of a MgH<sub>2</sub>-Al composite material. **Journal of Alloys and Compounds** **478 (2009) 273.**
- [14] C. Menapace, I. Lonardelli, M. Tait, A. Molinari. Nanostructured/Ultrafine multiphase steel with enhanced ductility obtained by mechanical alloying and Spark Plasma Sintering of powders. **Materials Science and Engineering A** **517 (2009) 1.**
- [15] I. Machado, I. Lonardelli, L. Girardini, A. Molinari. The study of ternary carbides formation during SPS consolidation process in the WC-Co-Steel system. **International Journal of Refractory and Hard Materials** **27 (2009) 883.**
- [16] M. Bortolotti, I. Lonardelli, L. Lutterotti. Rex: a computer program for structural analysis using powder diffraction data. **Journal of Applied Crystallography** **42 (2009) 538.**
- [17] J. Barreiro, J.R.M. Catalan, D. Prior, H.R. Wenk, S. Vogel, F. Diaz Garcia, R. Arenas, S. Sanchez Martinez, I. Lonardelli. Fabric development in a middle Devonian intraoceanic subduction regime: the Caréon Ophiolite (Northwest Spain). **Journal of Geology**, **118 (2010) 163.**
- [18] L. Lutterotti, M. Bortolotti, G. Ischia, I. Lonardelli, H.R. Wenk. Rietveld texture analysis from diffraction images. **Z. KRISTALL.**

**26 (2007) 125.**

- [19] L. Facchini, N. Vicente Jr., I. Lonardelli, E. Magalini, P. Robotti, A. Molinari. Metastable austenite in 17-4 Precipitation-Hardening stainless steel produced by selective laser melting. **Advanced Engineering Materials DOI 10.1002/adem.200900259 (in press).**
- [20] C. Menapace, I. Lonardelli, A. Molinari. Phase transformation in a nanostructured M300 maraging steel obtained by SPS of mechanically alloyed powders. **Journal of Thermal Analysis (2010) accepted.**

### **Papers published/submitted related to this PhD Thesis**

- [21] M. Zadra, F. Casari, I. Lonardelli, G. Ischia, A. Molinari. In situ precipitation of  $\text{Al}_2\text{O}_3$  and  $\text{k-Fe}_3\text{AlC}_{0.5}$  in iron aluminides through Spark Plasma Sintering: Microstructures and mechanical properties. **Intermetallics**, **15 (2007) 1650**.
- [22] I. Lonardelli, M. Zadra, G. Ischia, J. Gomez Barreiro, M. Bortolotti, A. Molinari. In situ high temperature Synchrotron diffraction experiments on Al-15%BN mechanically alloyed powder: observation of AlN nanoparticles precipitation and enhanced thermal stability of nanostructured Al matrix. **Journal of Alloys and Compounds** **486 (2009) 653**.
- [23] I. Lonardelli, J. Almer, G. Ischia, C. Menapace, A. Molinari. Deformation behavior in bulk Nanocrystalline-Ultrafine Aluminum: in situ evidence of plastic strain recovery. **Scripta Materialia** **60 (2009) 520**.
- [24] A. Molinari, I. Lonardelli, K. Demetrio, C. Menapace. On the thermal stability of nanostructured Al powder produced by cryomilling: dislocation density and second-phase particles controlling the grain growth. **Journal of Materials Science (2010) accepted**.
- [25] I. Lonardelli, J. Almer, M. Bortolotti, A. Molinari. In situ observations of stress-driven strain and texture recovery in bulk nc-UF Aluminum: explaining plastic deformation recovery. **Submitted to Science**

